

## Appendix A

# Charge Transfer Rates and Charge Transport

Here we provide supporting information for different molecular systems. P3HT:DIPBI (A.1), PPDI (A.2), PBDT-TS1:PPDI (A.3), PDTI (A.4), PHHP-AS (A.5), laddered nanoribbons (A.6), Pt complexes (A.7).

### A.1 P3HT:DIPBI

#### A.1.1 Charge Transfer Integrals for Hole Transfer

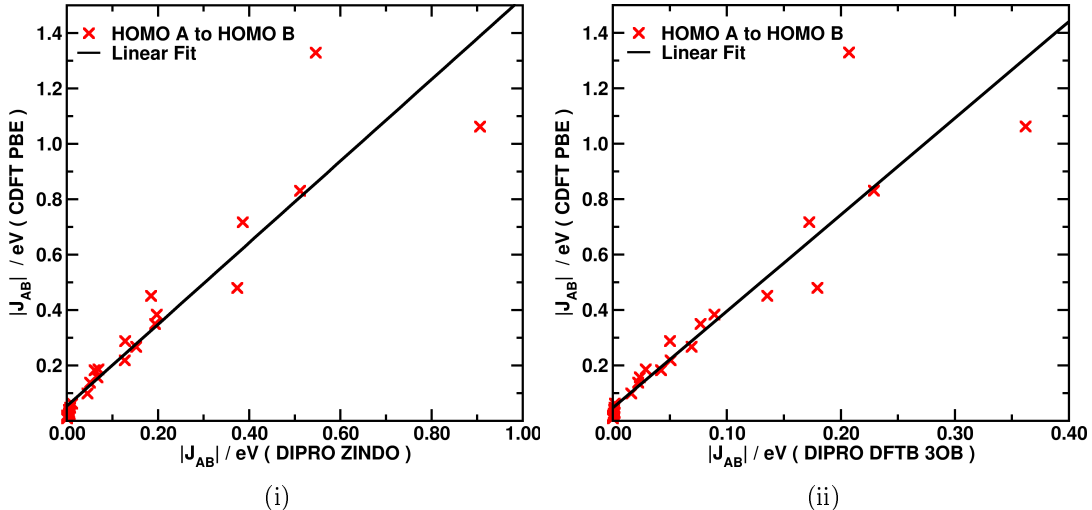


Figure A.1: Charge transfer integral  $|J_{AB}^h|$  for hole transfer in P3MT pairs of  $n = [3, 5, 7]$ . The DIPRO method in conjugation with ZINDO and DFTB/3OB-3-1 is scaled to CDFT/PBE/PW. The P3MT pairs are generated as co-facial oriented, planar segments  $\Delta x = 0 \text{ \AA}$  or with a lateral shift about  $\Delta x = 4 \text{ \AA}$  for various distances  $\Delta z = [3.0, 3.5, 4.0, 5.0, 6.0] \text{ \AA}$ .

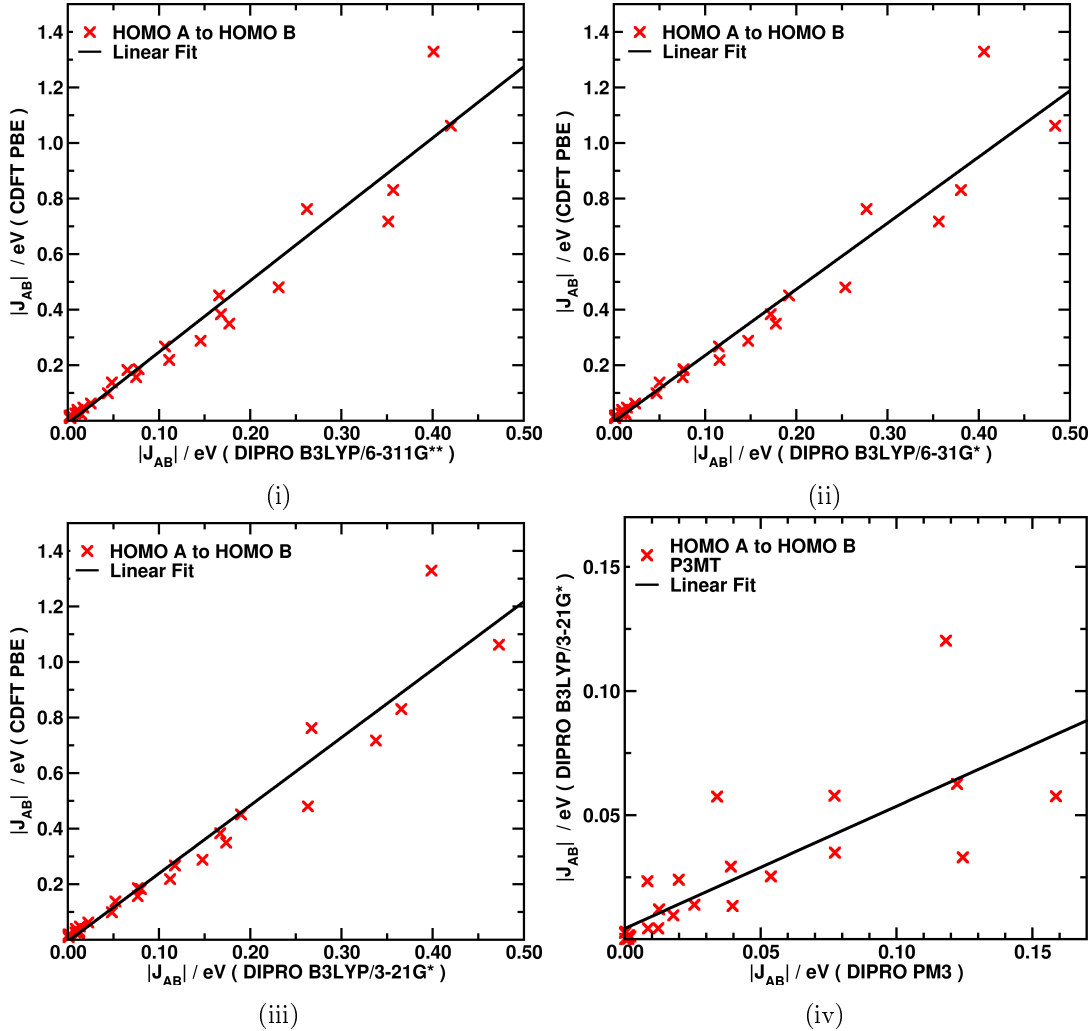


Figure A.2: Basis set dependence of the hole transfer integral  $|J_{AB}^h|$  for in P3MT  $n = [3, 5, 7]$ . The DIPRO/DFT data with (i) B3LYP/6-311G\*\*, (ii) B3LYP/6-31G\*, (iii) B3LYP/3-21G\* is compared to the CDFT/PBE/PW level of theory. Moreover, DIPRO PM3 data is scaled to B3LYP/3-21G\* (iv). The P3MT dimers are generated as planar segments with various distances [3.0, 3.5, 4.0, 5.0, 6.0] Å or with 3.0 Å and a lateral shift about 4 Å.

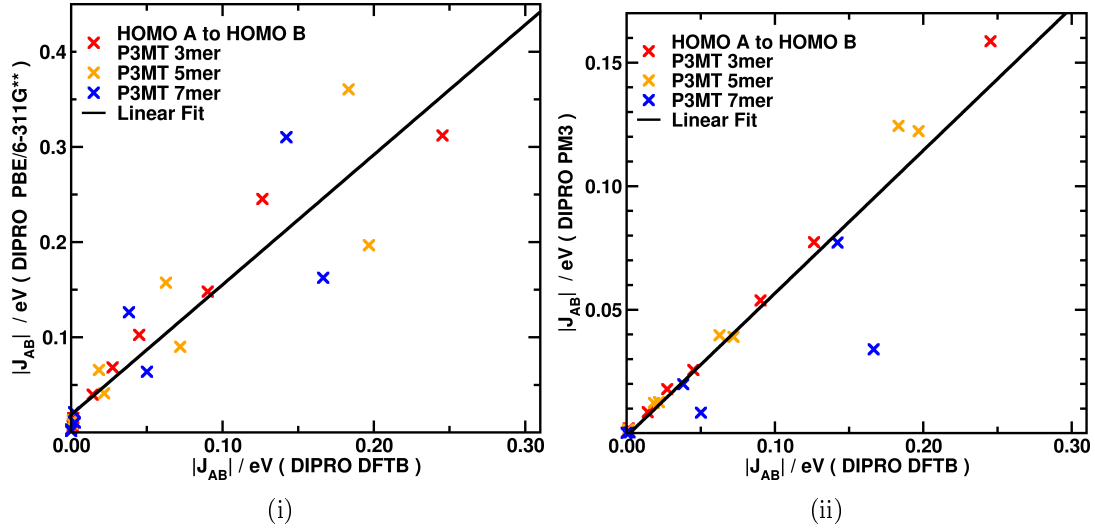


Figure A.3: The DIPRO/DFTB/Mio-1-1 data is scaled to (i) PBE/6-311G<sup>\*\*</sup> and (ii) PM3. The P3MT dimers are generated as planar segments with various distances [3.0,3.5,4.0,5.0,6.0] Å or with 3.0 Å and a lateral shift about 4 Å.

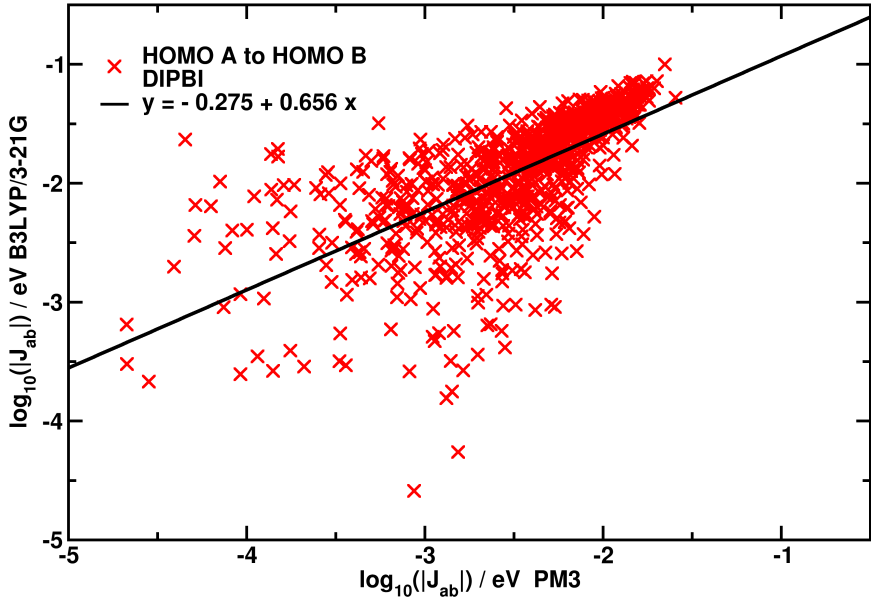


Figure A.4: Charge transfer integral  $|J_{AB}|$  in DIPBI/DIPBI dimers for hole transfer as HOMO A to HOMO B for the charge transfer integral  $|J_{AB}|_y$  with the DIPRO approach on B3LYP/3-21G level of theory and the semiempirical PM3 method  $|J_{AB}|_x$ . The 852 neighbouring DIPBI dimer pairs are extracted from the morphology at 500 K and exhibit a centre of mass distance in the range of  $d_{\text{COM}} = 2.0$  Å to  $d_{\text{COM}} = 8.0$  Å. The methods are scaled with a linear fit  $\log_{10} |J_{AB}|_y = 0.656 \times \log_{10} |J_{AB}|_x - 0.275$ . The graphic shows that the values can spread about 1.5 orders of magnitude, if the computationally cheaper PM3 is applied to parametrise DIPRO/DFT results.

### A.1.2 Charge Transfer Integrals for Electron Transfer

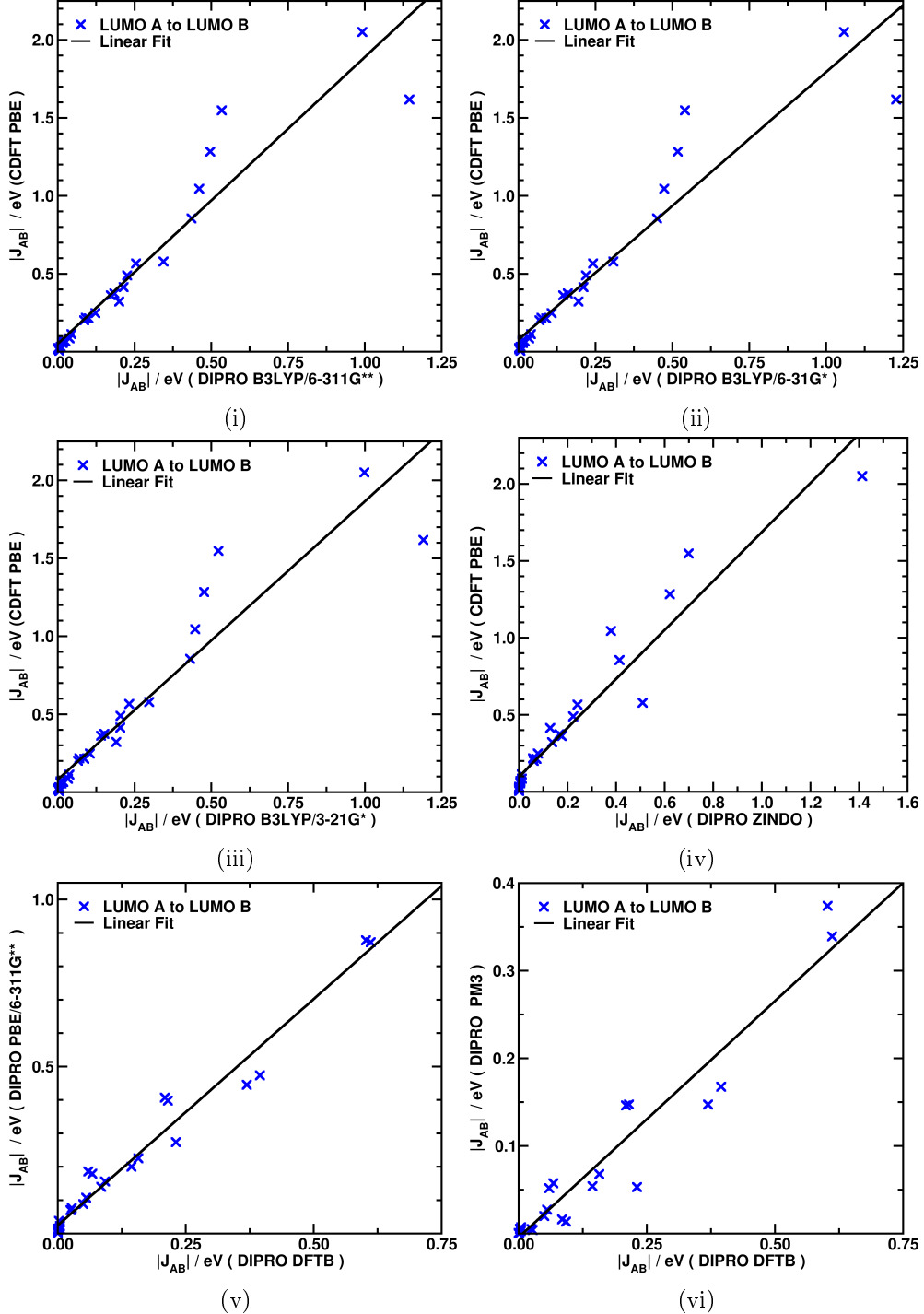


Figure A.5: Basis set dependence of the electron transfer integral  $|J_{AB}^e|$  for in P3MT  $n = [3, 5, 7]$  dimers. The DFT data with (i) B3LYP/6-311G\*\*, (ii) B3LYP/6-31G\*, (iii) B3LYP/3-21G\* is compared to the CDFT/PBE/PW level of theory. (iv) CDFT is plotted against DIPRO/ZINDO. The DIPRO/DFTB/Mio-1-1 data is scaled to (v) PBE/6-311G\*\* and (vi) PM3.

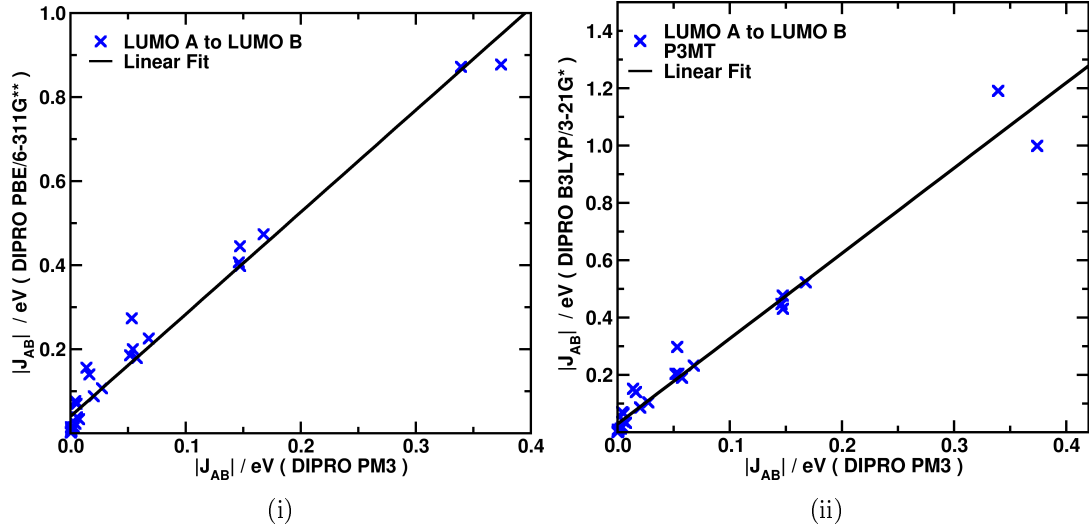


Figure A.6: The electron transfer integral  $|J_{AB}^e|$  in P3MT  $n = [3, 5, 7]$ . The DIPRO data in conjugation with PM3 is scaled to DIPRO/DFT results on (i) PBE/6-31G\*\* and (ii) B3LYP/3-21G\* level of theory. The P3MT dimers are generated as planar segments with various distances [3.0, 3.5, 4.0, 5.0, 6.0] Å or with 3.0 Å and a lateral shift about 4 Å.

### A.1.3 Geometric Parametrisation

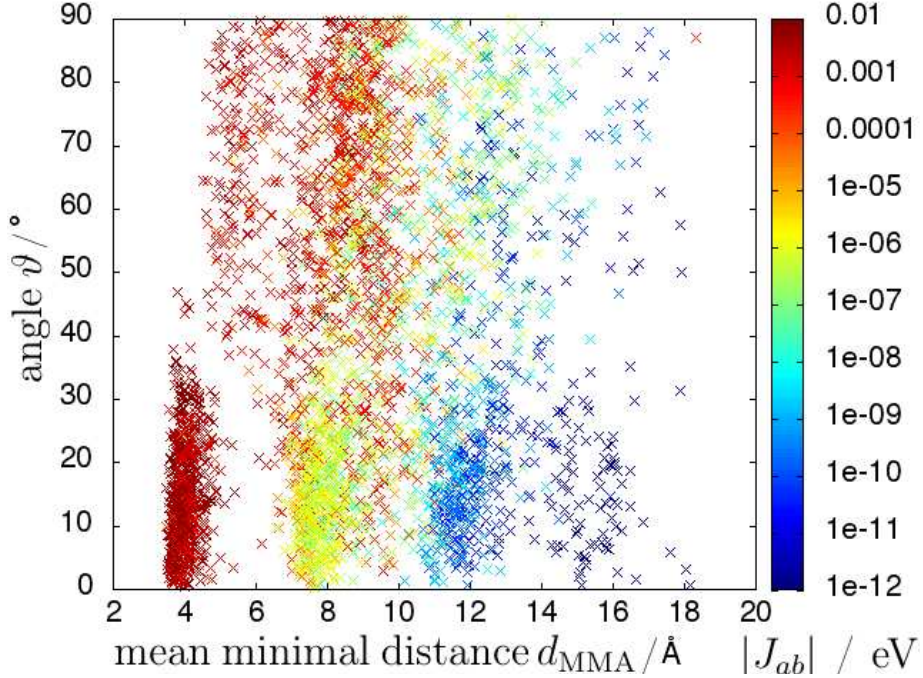


Figure A.7: The charge transfer integral  $|J_{AB}|$  between DIPBI/DIPBI dimers with the DIPRO/PM3 approach for hole transfer as a HOMO A to HOMO B transition as a function of the mean minimal distance  $d_{\text{MMA}}$ . The values for  $|J_{AB}| / \text{eV}$  are presented in a colour-coded schema and vary various orders of magnitude. The data displays 3752 DIPBI/DIPBI in the P3HT:DIPBI morphology at 500 K.

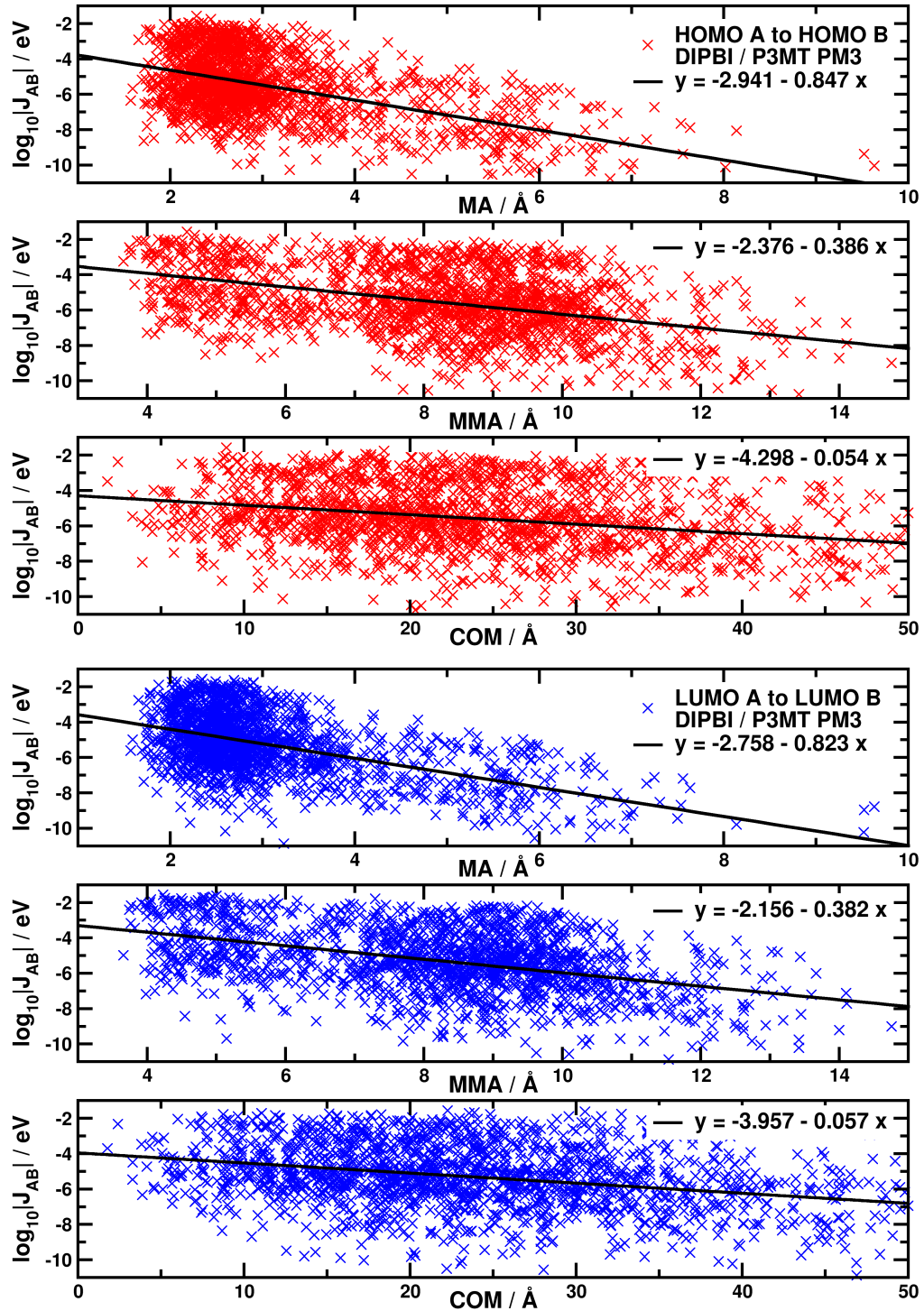


Figure A.8: A geometric parametrisation of the charge transfer integral  $\log_{10}|J_{AB}|$  between DIPBI/P3MT dimers with DIPRO/PM3 for hole transfer as a HOMO A to HOMO B transition (red) and for electron transfer DIPRO/PM3 as a LUMO A to LUMO B transition (blue) as a function of the minimal appearing distance  $d_{\text{MA}}$ , the mean minimal appearing distance  $d_{\text{MMA}}$  and the centre of mass distances  $d_{\text{COM}}$ . The DIPBI/P3MT dimers are extracted from the morphology at 500 K.

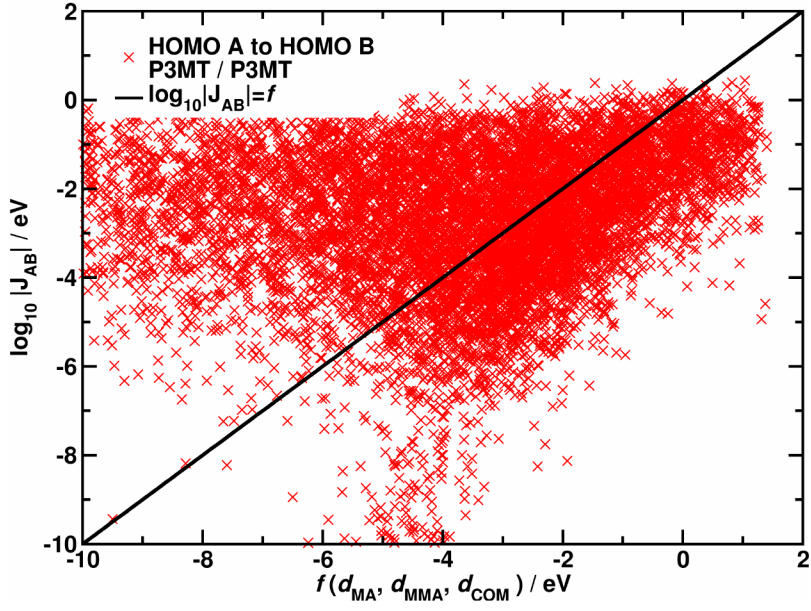


Figure A.9: The charge transfer integral  $\log_{10}|J_{AB}|$  for hole transfer (DIPRO/PM3) as a HOMO A to HOMO B transition between P3MT/P3MT pairs as a function the linear combination  $f(d_{\text{MA}}, d_{\text{MMA}}, d_{\text{COM}}) = A \cdot d_{\text{MA}} + B \cdot d_{\text{MMA}} + C \cdot d_{\text{COM}} + D$ . The optimised geometric parametrisation  $f$  depends on the minimal appearing distance  $d_{\text{MA}}$ , the mean minimal appearing distance  $d_{\text{MMA}}$  and the centre of mass distances  $d_{\text{COM}}$ .

#### A.1.4 Scaling the Overlap Integral

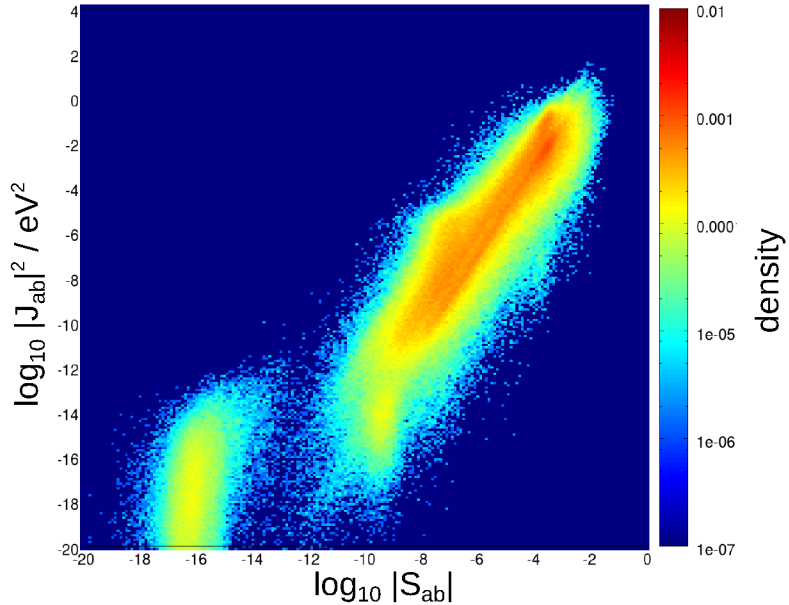


Figure A.10: Density plot of the charge transfer integral  $\log_{10} |J_{AB}|^2$  for electron transfer (DIPRO/PM3) as a function of the overlap  $\log_{10} |S_{AB}|$  for neighbouring  $\approx 4 \times 10^5$  charge transfer pairs in 12 distinct frames of P3HT:DIPBI morphologies.

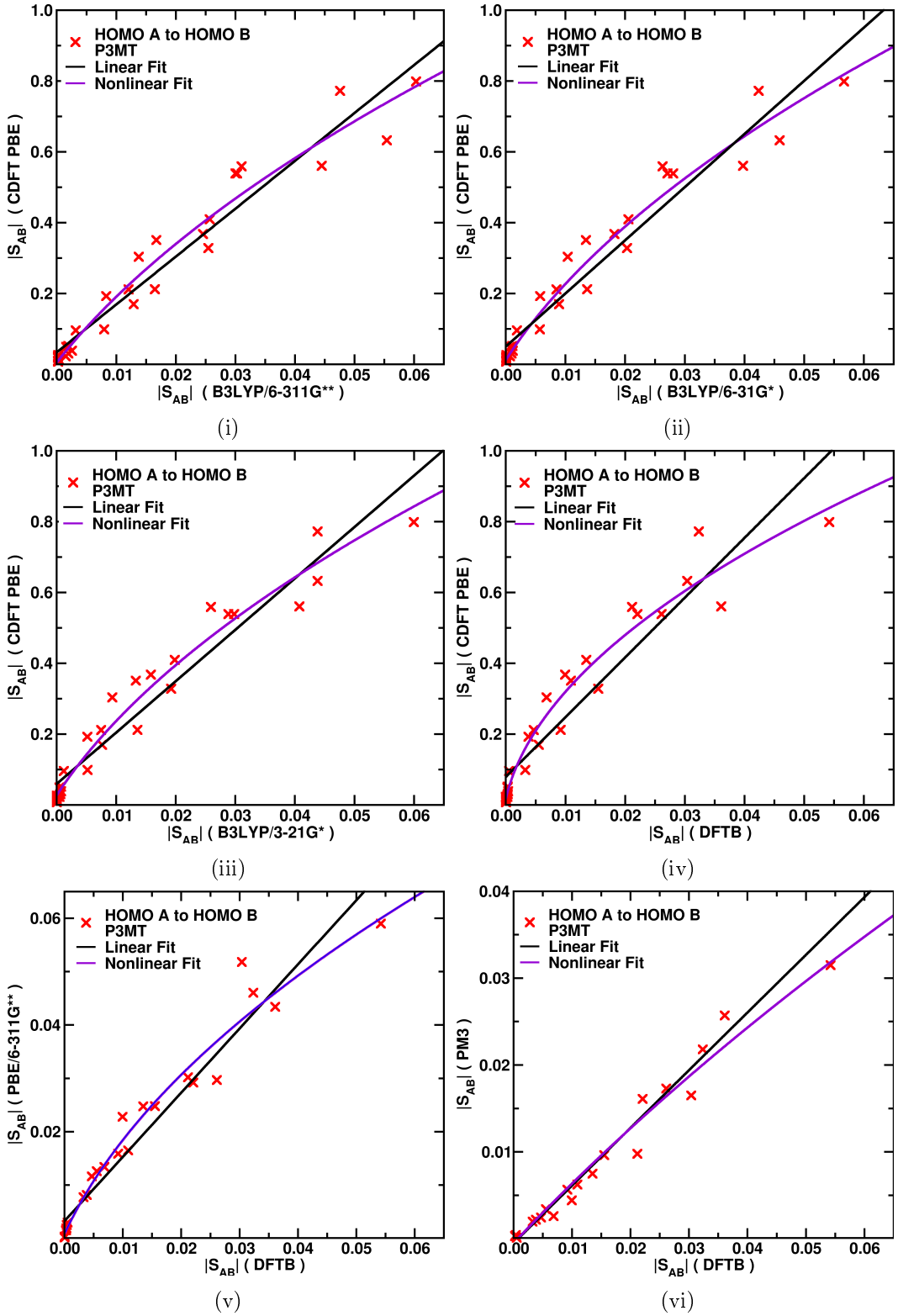


Figure A.11: Basis set dependence of the overlap  $|S_{AB}^h|$  for hole transfer in P3MT  $n = [3, 5, 7]$ . The DFT data with (i) B3LYP/6-311G\*\*, (ii) B3LYP/6-31G\*, (iii) B3LYP/3-21G\* is compared to the CDFT/PBE/PW level of theory. The DFTB/Mio-1-1 data is scaled to (iv) CDFT/PBE/PW, (v) PBE/6-311G\*\* and (vi) PM3. The P3MT dimers are generated as planar segments with various distances [3.0, 3.5, 4.0, 5.0, 6.0] Å or with 3.0 Å and a lateral shift about 4 Å. Linear and nonlinear fits are displayed for parametrisation.

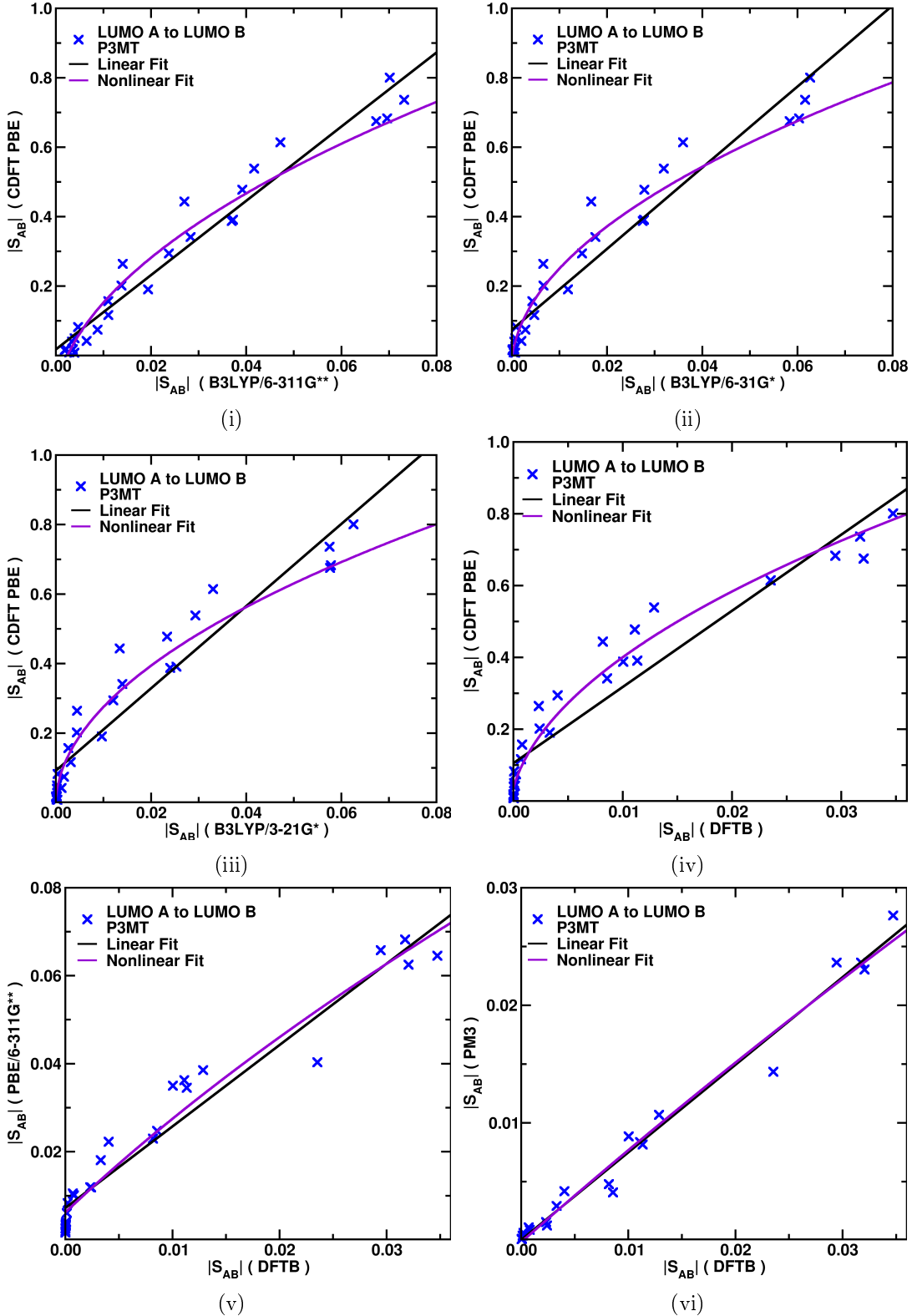


Figure A.12: Basis set dependence of the overlap  $|S_{AB}^e|$  for electron transfer in P3MT  $n = [3, 5, 7]$ . The DFT data with (i) B3LYP/6-311G\*\*, (ii) B3LYP/6-31G\*, (iii) B3LYP/3-21G\* is compared to the CDFT/PBE/PW level of theory. The DFTB/Mio-1-1 data is scaled to (iv) CDFT/PBE/PW, (v) PBE/6-311G\*\* and (vi) PM3. The P3MT dimers are generated as planar segments with various distances [3.0, 3.5, 4.0, 5.0, 6.0] Å or with 3.0 Å and a lateral shift about 4 Å. Linear and nonlinear fits are displayed for parametrisation.

### A.1.5 Transfer Rates and Nearest Neighbour Cutoff

We focus on an outtake from the P3HT:DIPBI morphology (Fig. 3.29) as an example. If we employ a cutoff radius  $r_{\text{cut}}^{\text{NN}} = 20 \text{ \AA}$  using the  $|\mathbf{d}_{\text{RCOM}}|$  distance around the central DIPBI molecule, we obtain  $N^{\text{NN}} = 32$  neighbouring hopping sites. Taking a closer look at the Marcus electron transfer rates from the DIPBI to hopping sites in the vicinity (Fig. A.13), reveals huge alternations in  $k_{\text{AB}}^e$  that cover many orders of magnitude. Even if two neighbours possess similar distance to the DIPBI, their transfer rates can even vary a lot. The general trend indicates a decay of  $k_{\text{AB}}^e$  with rising  $d_{\text{AB}}$ . However, we find a local maximum in the rates at  $d_{\text{AB}} \approx 18 \text{ \AA}$ . This is where the  $\Delta E^{\text{ext}}$  term balances the other components in the exponent of the Marcus rate expression.

The total escape rate  $k^{\text{esc}}$  for an electron on the selected DIPBI site is dominated by the rate  $k^e = 5.00 \times 10^{16} \text{ s}^{-1}$  to the closest DIPBI. If more neighbours are taken into account, the total escape rate  $k^{\text{esc}}$  does not change significantly. Hence, the probability of jumping to the adjacent DIPBI remains at a high level  $p = 99.99\%$ . In this case, an increase in  $r_{\text{cut}}^{\text{NN}}$  only increases the number of rare events, which can occur but are hardly sampled in kMC simulations.

If we focus on a P3HT segment with thiophene chain length  $n = 6$  on an embedded polymer chain in the P3HT:DIPBI morphology, we observe a similar behaviour (Fig. A.13). In this case, the segment is sandwiched between two neighbouring P3HT with  $n = 3$  each. These segments are accessible by high intramolecular hole transfer rates  $k_{\text{AB}}^h = 5.78 \times 10^{12} \text{ s}^{-1}$  and  $k_{\text{AB}}^h = 1.74 \times 10^{13} \text{ s}^{-1}$ , whereas lower intermolecular rates connect all other neighbours. The hole escapes the  $n = 6$  segment with a high probability  $p = 66.63\%$  to the second neighbour and  $p = 33.20\%$  to the first. It can escape the polymer chain from this segment with a probability of  $p = 0.08\%$  to the neighbour with index 10 and  $p = 0.10\%$  to index 12. Here, the local maximum in the rates is at  $d_{\text{AB}} \approx 13.8 \text{ \AA}$ . The rate  $k^{\text{esc}}$  converges quickly to  $k^{\text{esc}} = 1.74 \times 10^{13} \text{ s}^{-1}$  for the P3HT segment.

Since  $k^{\text{esc}}$  does not change significantly with an increase in the number of neighbours considered, a cutoff of  $N_{\text{cut}}^{\text{NN}} = 12$  is sufficient as a tradeoff between accuracy and computational effort. This choice corresponds approximately to a cutoff radius of  $r_{\text{cut}}^{\text{NN}} \approx 15 \text{ \AA}$ . Even though a few rates only dominate the total escape rates, also rare events with small  $k_{\text{AB}}$  need to be taken into account to capture the correct charge carrier dynamics.

### A.1.6 kMC Simulations

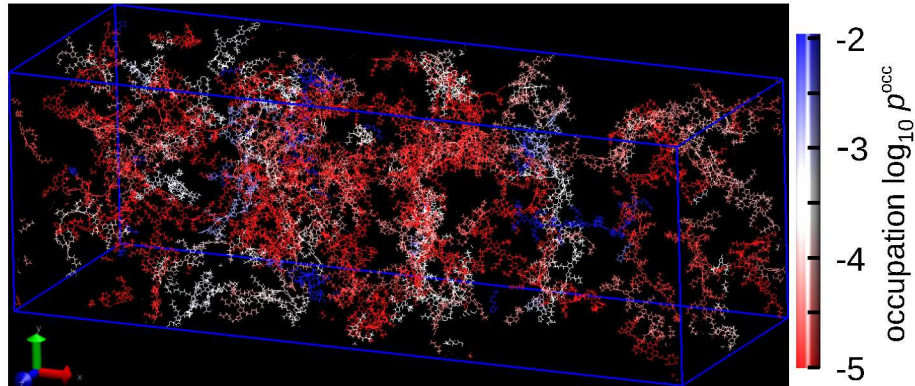


Figure A.14: Hopping sites with 10% highest occupation numbers in P3HT morphologies.

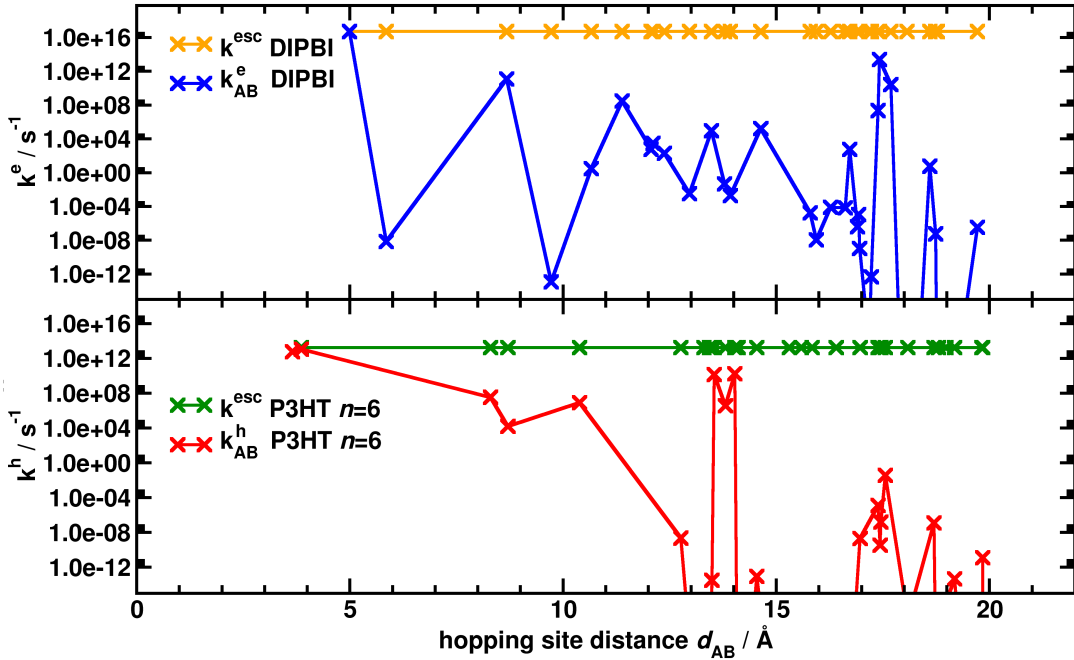


Figure A.13: Dependence of the total escape rate  $k^{esc}$  and Marcus charge transfer rates  $k_{AB}^e$  and  $k_{AB}^h$  for electron and hole transfer including the nearest neighbours within a radius  $r_{cut}^{NN} = 20 \text{ \AA}$  around a central hopping site for a DIPBI molecule (upper panel) and a P3HT segment  $n = 6$  (lower panel). The rates are displayed as a function of the hopping site distance  $|d_{RCOM}|$ .  $k^{esc}$  converges quickly to  $k^{esc} = 5.00 \times 10^{16} \text{ s}^{-1}$  for the DIPBI and to  $k^{esc} = 1.74 \times 10^{13} \text{ s}^{-1}$  for the P3HT segment. The data points are connected to emphasise the alternations and to highlight the presence of low rates, which are outside of the displayed plotting range.

Table A.1: Mobility  $\mu_z$  and associated standard deviation  $\sigma_z$  based on single charge carrier kMC simulations with intramolecular and intermolecular transfer for hole transport. We apply a fixed external field  $\mathbf{F}_z^{\text{ext}} = 1.0 \times 10^7 \frac{\text{V}}{\text{m}}$  to the P3HT:DIPBI blend.  $N_{\text{kmc}} = 512$  trajectories were sampled with the same initial charge injection sites. The number of simulation steps is  $N_{\text{steps}} = 1.0 \times 10^6$  to  $1.0 \times 10^{10}$ .

$N_{\text{kmc}} = 100$  trajectories were sampled with  $N_{\text{steps}} = 1.0 \times 10^{11}$ . The applied Marcus rates include  $|J_{AB}|$ (DIPRO/PM3),  $\lambda^{\text{in}}$  and  $\Delta E^{\text{in}}$  (B3LYP/6-311G\*\*)  $\lambda^{\text{out}} = 0.0 \text{ eV}$ ,  $\Delta E^{\text{out}} = 0.0 \text{ eV}$ .

$N_{\text{steps}}$	$\mu_z$ [ $\text{cm}^2/\text{Vs}$ ]	$\sigma_z$ [ $\text{cm}^2/\text{Vs}$ ]
1.0E6	7.4649E-3	2.707E-3
1.0E7	7.5243E-3	9.065E-4
1.0E8	7.4872E-3	2.568E-4
1.0E9	7.4972E-3	8.744E-5
1.0E10	7.4957E-3	2.825E-5
1.0E11	7.4944E-3	8.823E-6

Table A.2: Mean values of the charge transfer integrals  $\log_{10}|J_{AB}|^2$  and standard deviation  $\log_{10}\sigma$  of the distributions for hole transfer in an amorphous, segmented P3HT morphology using ZINDO/MOO or DIPRO in conjugation with DFTB/3OB or different semiempirical methods PM3, AM1, ZINDO.

method	$\log_{10}( J_{AB} ^2/\text{eV}^2)$	$\log_{10}(\sigma/\text{eV}^2)$
PM3	-6.38	5.54
AM1	-7.58	5.15
DFTB/3OB	-8.02	3.07
B3LYP/6-31G*	-9.22	4.67
ZINDO	-9.96	4.52
ZINDO/MOO	-14.15	8.79

Table A.3: Comparison of three P3HT:DIPBI morphologies based on different annealing temperatures 500 K, 700 K, and 900 K. The number of hopping sites and charge transfer (CT) pairs for intermolecular and intramolecular transitions are listed including the 12 nearest neighbours (NN). The P3HT polymer chains are partitioned using  $\theta_{\text{SCCS}}^{\text{cut}} = 75^\circ$ . Average hopping site distance  $\bar{d}_{AB}$  taking all transitions into account, and an average distance of the 12th nearest neighbour  $\bar{d}_{NN12}$  for all sites and around DIPBI molecules  $\bar{d}_{NN12}^{\text{DIPBI}}$  and P3HT segments  $\bar{d}_{NN12}^{\text{P3HT}}$ .

	morphologies		
	500 K	700 K	900 K
hopping sites	6515	6575	6457
DIPBI molecules	1248	1248	1248
P3HT segments	5267	5327	5209
total number of CT pairs	47546	47869	47126
DIPBI $\leftrightarrow$ DIPBI	3496	3544	2097
DIPBI $\leftrightarrow$ P3HT	8726	8687	11290
P3HT $\leftrightarrow$ P3HT	35324	35638	33739
P3HT $\leftrightarrow$ P3HT intramolecular	4851	4911	4793
P3HT $\leftrightarrow$ P3HT intermolecular	30473	30727	28946
All intermolecular CT pairs	42695	42958	42333
$\bar{d}_{AB}$ [Å]	$8.42 \pm 3.07$	$8.38 \pm 3.20$	$8.51 \pm 3.10$
$\bar{d}_{NN12}$ [Å]	$11.49 \pm 2.11$	$11.46 \pm 2.43$	$11.61 \pm 2.01$
$\bar{d}_{NN12}^{\text{DIPBI}}$ [Å]	$14.21 \pm 1.51$	$15.10 \pm 1.71$	$14.19 \pm 1.44$
$\bar{d}_{NN12}^{\text{P3HT}}$ [Å]	$10.80 \pm 1.57$	$10.61 \pm 1.57$	$11.03 \pm 1.60$

### A.1.7 DIPBI Aggregation

In order to analyse the aggregation patterns of DIPBI in the P3HT:DIPBI morphologies, we define a geometric centre  $\mathbf{d}_A$  for every DIPBI located in between two C atoms (see green dot and adjacent C atoms (Fig. A.15)) and define a molecular plane, which is given by four distance vectors  $\mathbf{R}_1, \mathbf{R}_2, \mathbf{R}_3, \mathbf{R}_4$  and then we determine four associated normal vector  $\mathbf{n}_i$ ,

$$\mathbf{n}_1 = \frac{\mathbf{R}_1 \times \mathbf{R}_2}{\mathbf{R}_1 \cdot \mathbf{R}_2}, \quad \mathbf{n}_2 = \frac{\mathbf{R}_2 \times \mathbf{R}_3}{\mathbf{R}_2 \cdot \mathbf{R}_3}, \quad \mathbf{n}_3 = \frac{\mathbf{R}_1 \times \mathbf{R}_4}{\mathbf{R}_1 \cdot \mathbf{R}_4}, \quad \mathbf{n}_4 = \frac{\mathbf{R}_3 \times \mathbf{R}_1}{\mathbf{R}_3 \cdot \mathbf{R}_1}. \quad (288)$$

The normal vector  $\mathbf{n}_A^{\text{DIPBI}}$  is the average of these four normal vectors  $\mathbf{n}_i$  as follows

$$\mathbf{n}_A^{\text{DIPBI}} = \frac{\sum_i^4 \mathbf{n}_i}{|\sum_i^4 \mathbf{n}_i|}. \quad (289)$$

A visual definition of the vectors  $\mathbf{R}_1, \mathbf{R}_2, \mathbf{R}_3, \mathbf{R}_4$  and corresponding normal vector  $\mathbf{n}_A^{\text{DIPBI}}$  is depicted in Figure A.15 for a selected DIPBI (green vector).

We calculate the intermolecular distance  $d_{AB} = |\mathbf{d}_B - \mathbf{d}_A|$  and the enclosed angle  $\alpha = \arccos(\mathbf{n}_A^{\text{DIPBI}} \cdot \mathbf{n}_B^{\text{DIPBI}})$  for every adjacent DIPBI molecule B in the vicinity of A ( $r_{\text{COM}}^{\text{cut}} = 15 \text{ \AA}$ ) in order to characterise the relative orientation of two DIPBI molecules. The density plots demonstrate the frequency of occurrence of distinct relative DIPBI/DIPBI arrangements as a function of  $d_{AB}$  and  $\alpha$  in the simulation box (Fig. A.15).

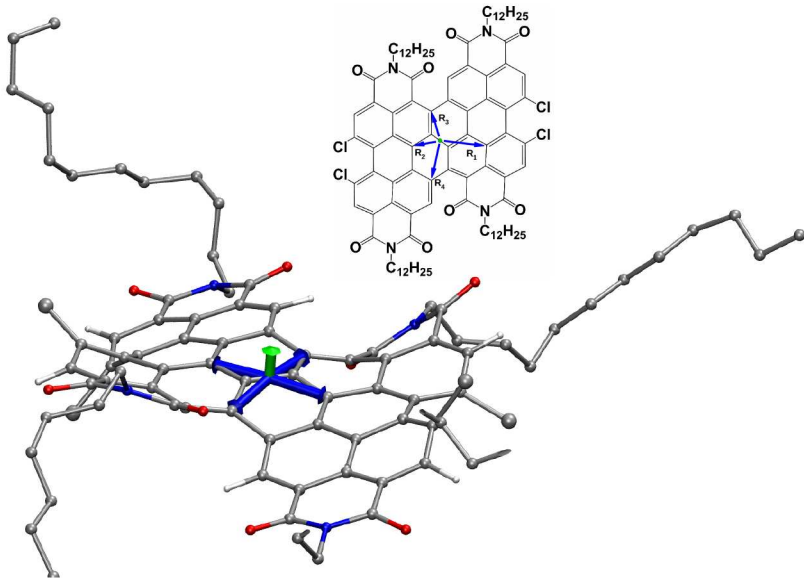


Figure A.15: Selected DIPBI and normal vector  $\mathbf{n}_A^{\text{DIPBI}}$  (green vector). The inset shows the chemical structure and the vectors  $\mathbf{R}_1, \mathbf{R}_2, \mathbf{R}_3, \mathbf{R}_4$  (blue vectors) pointing from the geometric centre (green circle) to carbon atoms in the vicinity to define a molecular plane.

### A.1.8 Distributions of Site Energies and Outer-sphere Reorganization Energy

The on-site energy contributions  $E_i = E^{\text{el}} + E^{\text{pol}}$  for 416 P3HT chains using the Thole model (Fig. A.16) lead to an average energy  $\bar{E}_i^h = (-0.131 \pm 0.146)$  eV for hole transport. Here, no partitioning of the P3HT 32mer polymer chains is employed. Moreover, the outer-sphere reorganization energy distribution is centred at  $\bar{\lambda}_h^{\text{out}} = (0.157 \pm 0.014)$  eV for hole transport.

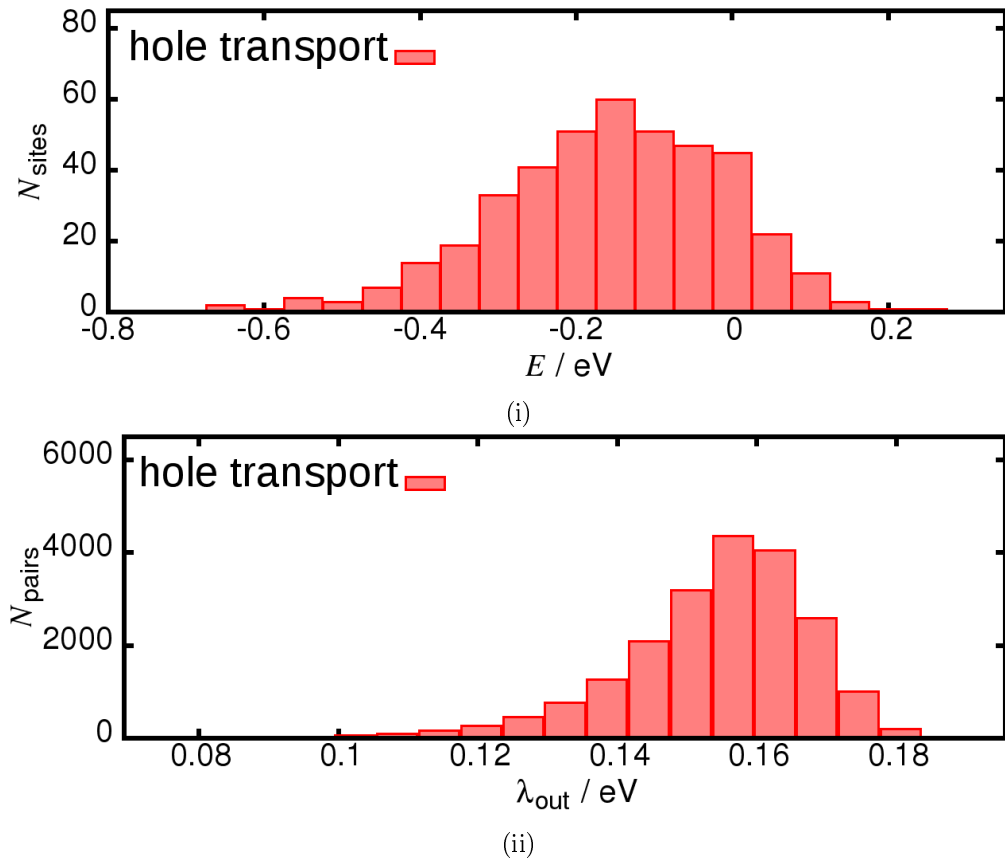


Figure A.16: Distribution of on-site energy contributions  $E_i = E^{\text{el}} + E^{\text{pol}}$  (Eq. 235 and 241) in unpartitioned P3HT  $n=32$  using the Thole model (i).

Distribution of the outer-sphere reorganization energy  $\lambda^{\text{out}}$  (Eq. 231) for charge transfer pairs  $N_{\text{pairs}}$  P3HT  $n=32$  in a morphology with 416 P3HT chains (ii).

If we take all transitions into account and determine the distribution of the site-energy differences  $\Delta E_{AB}^h$  in P3MT (Fig. A.17a,i) and P3HT (Fig. A.17b,ii). We find a broader distribution  $\Delta \bar{E}_{AB}^h = (6.4 \pm 209.9)$  meV in P3HT( $n=32$ ) than in P3MT( $n=32$ )  $\Delta \bar{E}_{AB}^h = (2.3 \pm 106.6)$  meV. The width of the distribution, the energetic disorder, is about twice as large in P3HT as when the side chains in P3MT are neglected. The same trend applies to electron transfer, where we find  $\Delta \bar{E}_{AB}^h = (0.6 \pm 182.9)$  meV for P3HT and  $\Delta \bar{E}_{AB}^h = (-0.8 \pm 108.1)$  meV for P3MT.

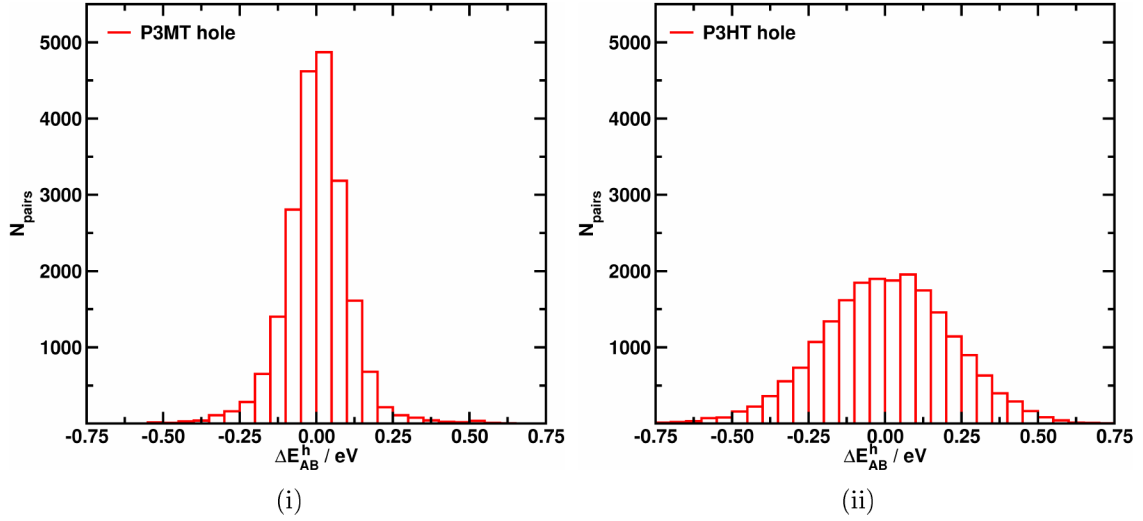


Figure A.17: Distribution of site-energy differences  $\Delta E_{AB}^h$  in P3MT (left) and P3HT (right) with thiophene segment length  $n = 32$  using the Thole model in a morphology with 416 P3HT chains. They are determined for neighbouring pairs  $N_{\text{pairs}}$  using a cutoff radius  $r_{\text{NN}}^{\text{cut}} = 20 \text{ \AA}$ . P3HT yields a broader distribution  $\bar{\Delta E}_{AB}^h = (6.4 \pm 209.9) \text{ meV}$  when compared to P3MT  $\bar{\Delta E}_{AB}^h = (2.3 \pm 106.6) \text{ meV}$ .

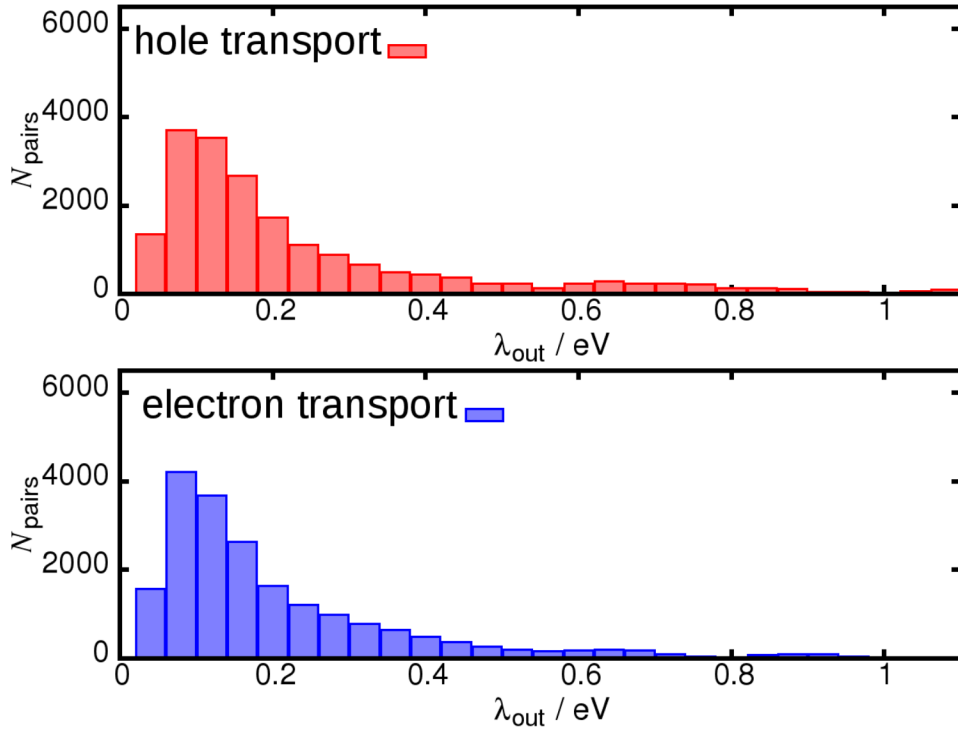


Figure A.18: Distribution of the outer-sphere reorganization energy  $\lambda_{\text{out}}$  for positively and negatively charged hopping pairs in P3MT ( $n = 32$ ). The Pakar factor is  $c_p = 0.1$ .

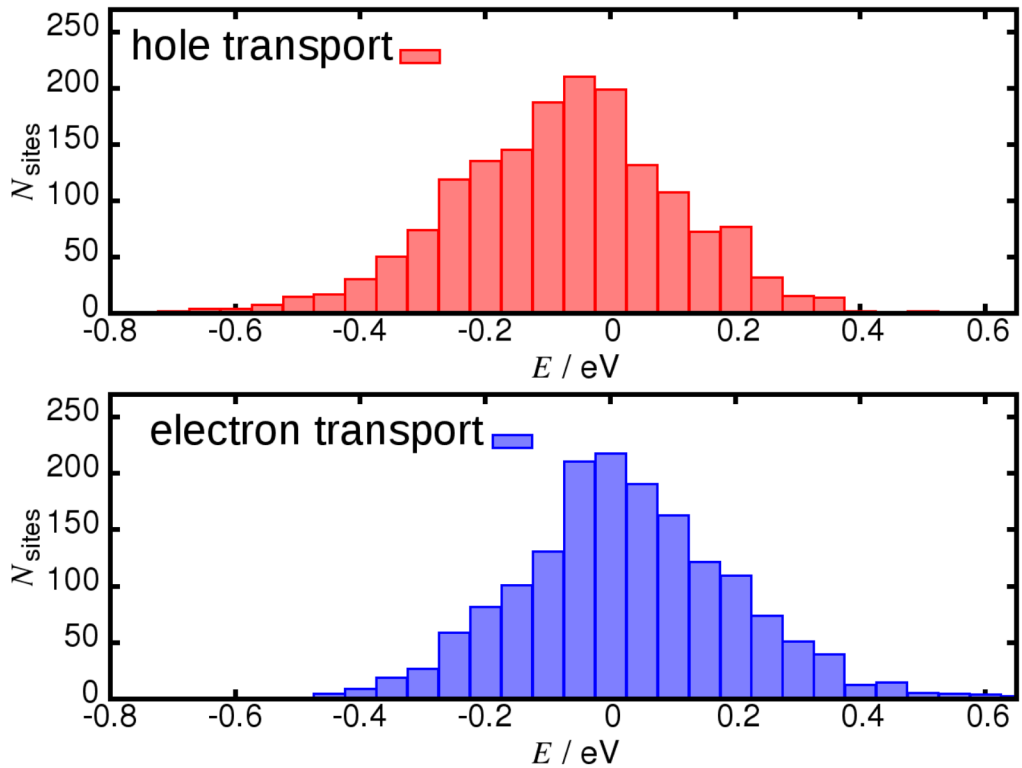


Figure A.19: On-site energy contributions  $E_i = E^{\text{el}} + E^{\text{pol}}$  (Eq. 235 and 241) for hole or electron transport from multipole analysis using the Thole model (left).

In the following model, the morphology of a single frame from a DIPBI/P3HT blend at 500 K annealing temperature is selected and a model two component system with 1248 DIPBI molecules and 416 P3HT polymers, which are treated as a single molecules with  $n = 32$  thiophene units.

A neighbour is added to the neighbour list, if two DIPBI molecules are within a cutoff radius  $r_{\text{NN}}^{\text{cut}} = 1.3$  nm and a P3HT chain is added if the centre is within  $r_{\text{NN}}^{\text{cut}} = 1.8$  nm. This choice results in 2885 DIPBI/DIPBI pairs, 735 P3HT( $n = 32$ )/P3HT( $n = 32$ ) and 2530 DIPBI/P3HT( $n = 32$ ) hetero-molecular hopping pairs and therefore one gets in total  $N_{\text{pairs}} = 6150$  hopping pairs inside the morphology. As no segmentation of the polymer chain is applied, only intermolecular charge transfer is present in this model.

The distributions for the on-site energies including the multipole analysis with the Thole model are centred for holes to at  $\bar{E}^{\text{h}} = (-0.038 \pm 0.189)$  eV and for electrons at  $\bar{E}^{\text{e}} = (0.041 \pm 0.188)$  eV, respectively. The distributions for the outer-sphere reorganization energies do not differ significantly for holes with  $\bar{\lambda}_{\text{out}}^{\text{h}} = (0.074 \pm 0.048)$  eV and electrons  $\bar{\lambda}_{\text{out}}^{\text{e}} = (0.073 \pm 0.048)$  eV (Fig. A.19).

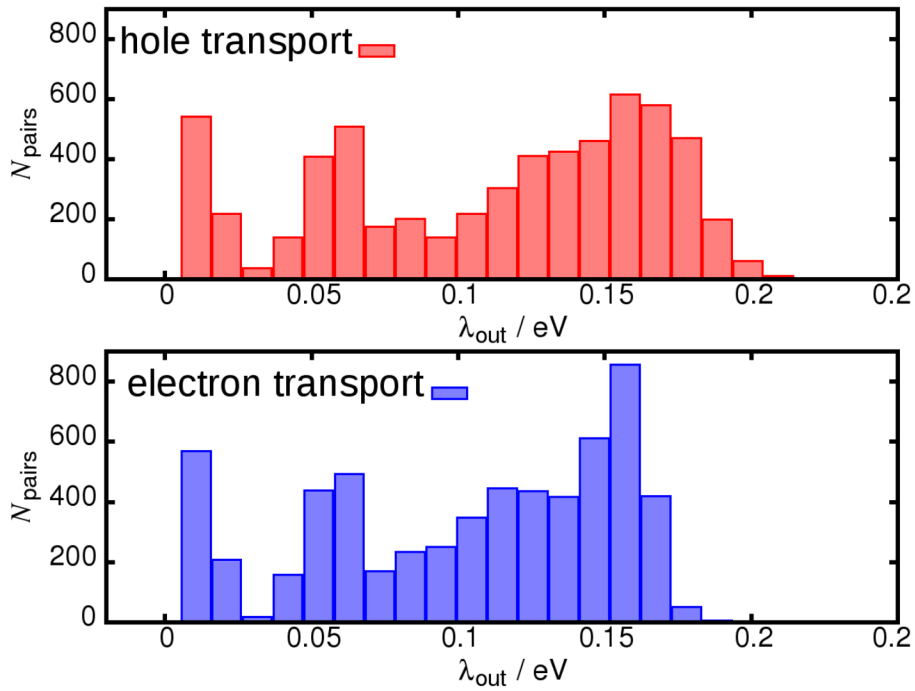


Figure A.20: Distribution of the outer-sphere reorganization energy  $\lambda_{\text{out}}$  for positively and negatively charged hopping pairs in a morphology with 1248 DIPBI and 416 P3HT chains with segment length ( $n=32$ ). The Pakar factor is  $c_p = 0.1$ .

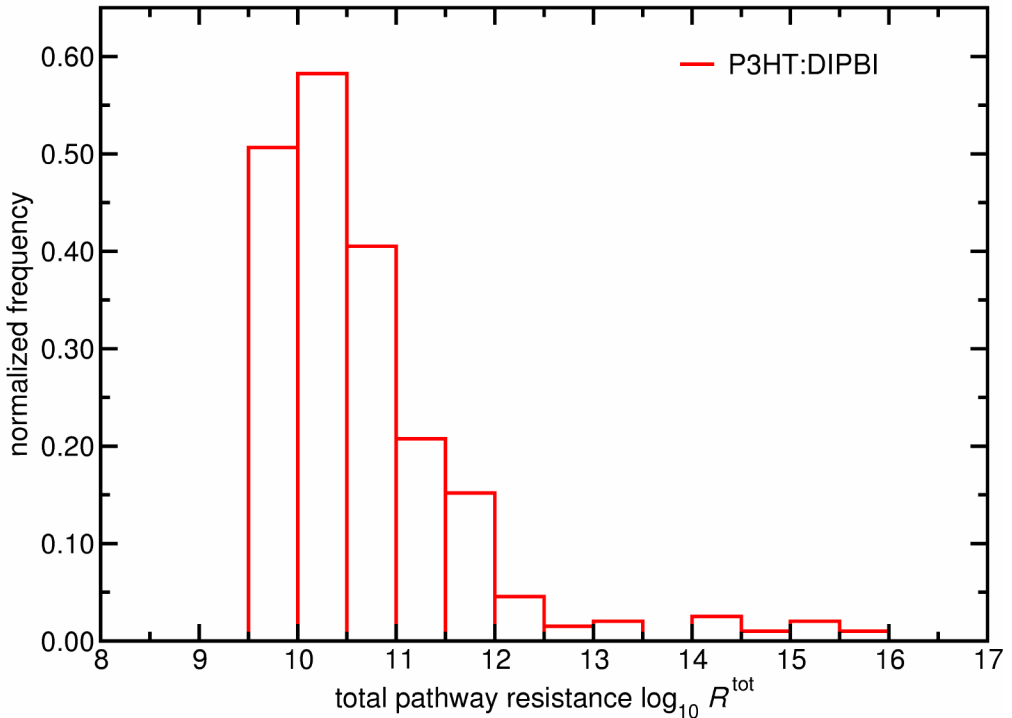


Figure A.21: Distribution of the total resistance  $\log_{10} R^{\text{tot}}$  for hole transport pathways in P3HT:DIPBI morphology using the Dijkstra algorithm.

## A.2 PPDI

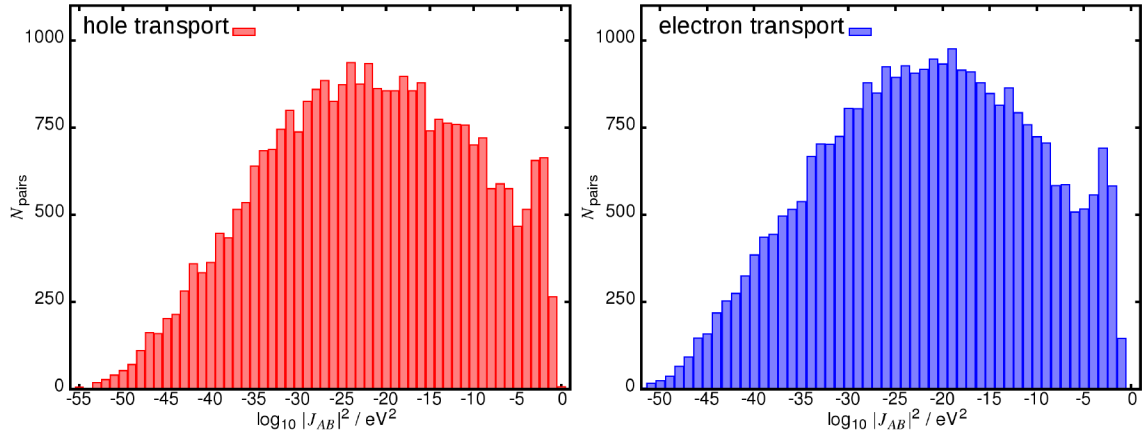


Figure A.22: Charge transfer integral  $|J_{AB}|^2$  for hole (left) and electron transfer (right) with ZINDO/MOO in PPDI morphology with 800 molecules.

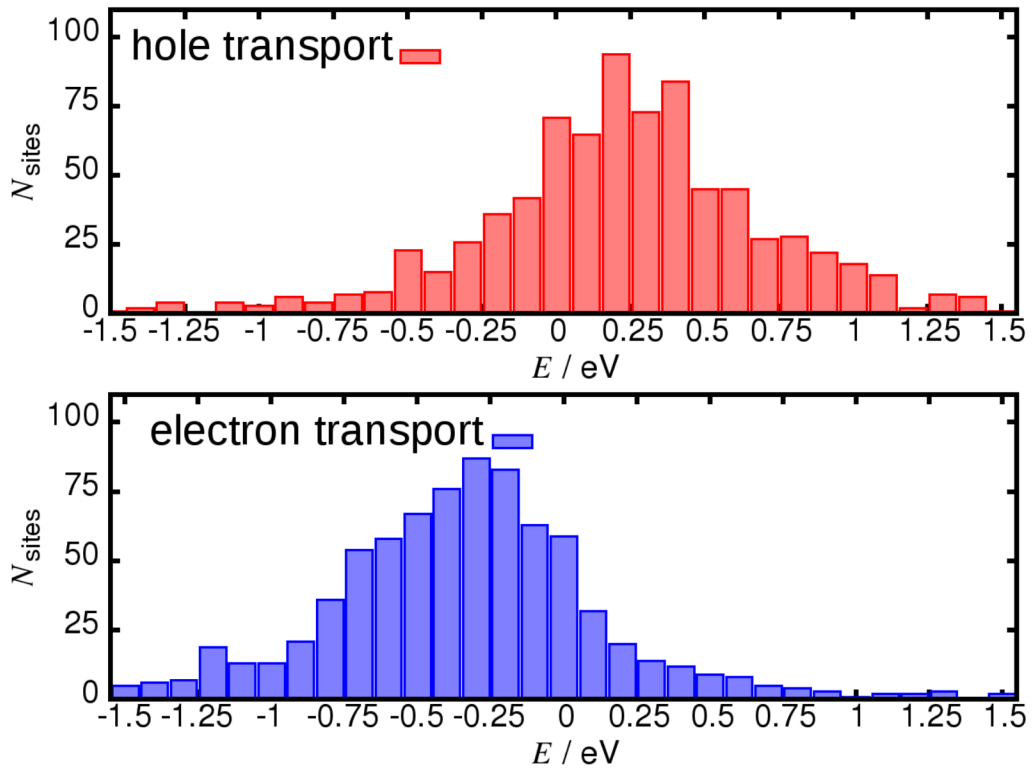


Figure A.23: Site-energy contributions  $E$  for hole or electron transport in PPDI using the Thole model (left).

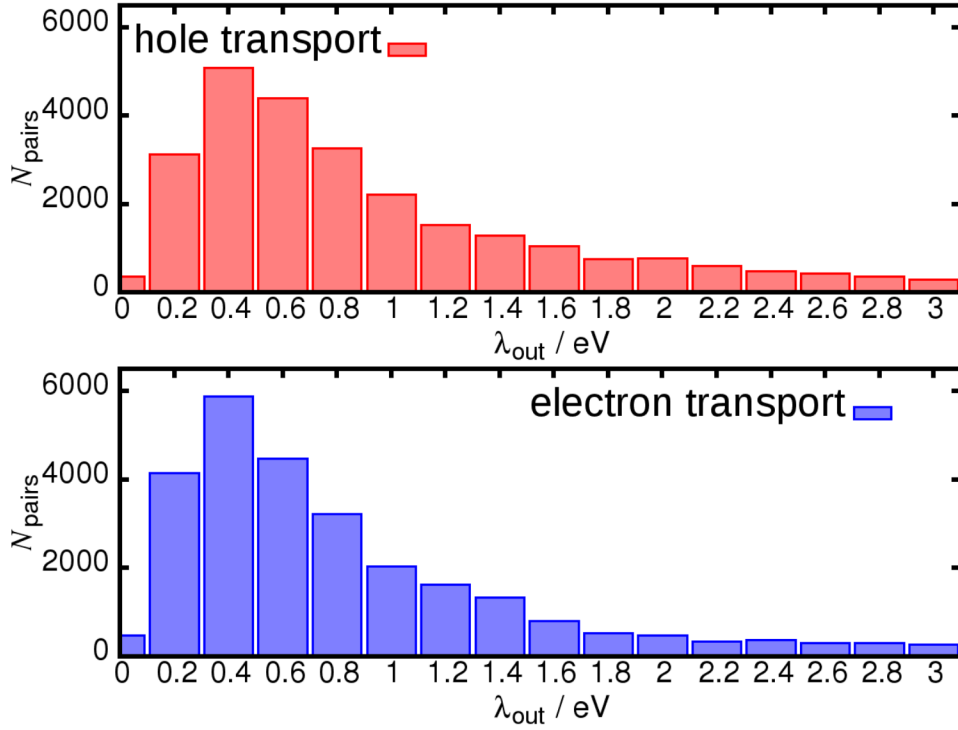


Figure A.24: Distribution of the outer-sphere reorganization energy  $\lambda_{\text{out}}$  for a positively and negatively charged PPDI in a morphology with 800 molecules.

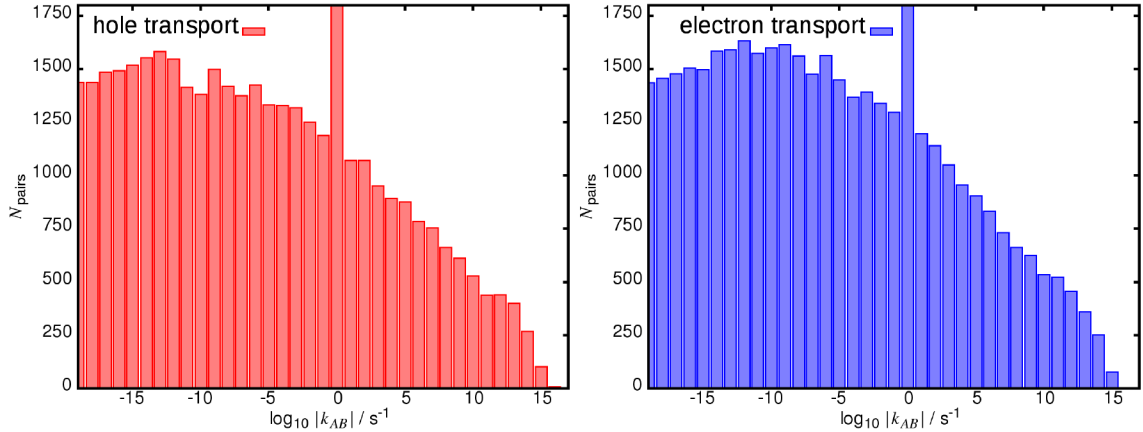


Figure A.25: Marcus charge transfer rates  $\log_{10} k_{AB}$  for hole (left) and electron transport (right) with  $|J_{AB}|$  (ZINDO/MOO),  $\lambda^{\text{in}}$  (B3LYP/6-311G\*\*),  $\lambda^{\text{out}}$ ,  $\Delta E^{\text{out}}$ , in PPDI morphology with 800 molecules. Marcus charge transfer rates with  $k < 1.0 \times 10^{-20} \text{ s}^{-1}$  are set to zero.

### A.3 PBDT-TS1:PPDI

In SI Fig. A.26 the Kohn-Sham frontier energies are depicted as a function of the chain length in the PBDT-TS1. The frontier orbitals are not degenerated energetically. The energy gap reveals a decrease with an increase in the system length, which is in line with the  $L^{-1}$ -dependence of the energy for a particle in a one-dimensional box of length  $L$  [419, 420].

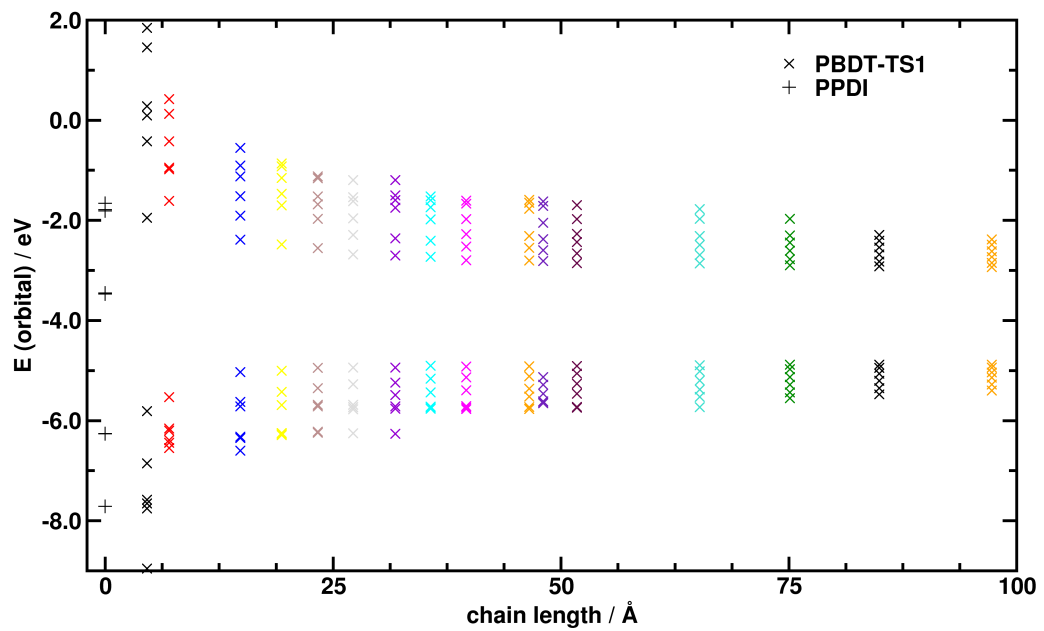


Figure A.26: Kohn-Sham frontier orbital energies in eV for PPDI, the subunits (A) and (B) and PBDT-TS1 polymer as a function of the polymer chain length at the optimised ground state  $S_0$  geometry (B3LYP/6-31G\*).

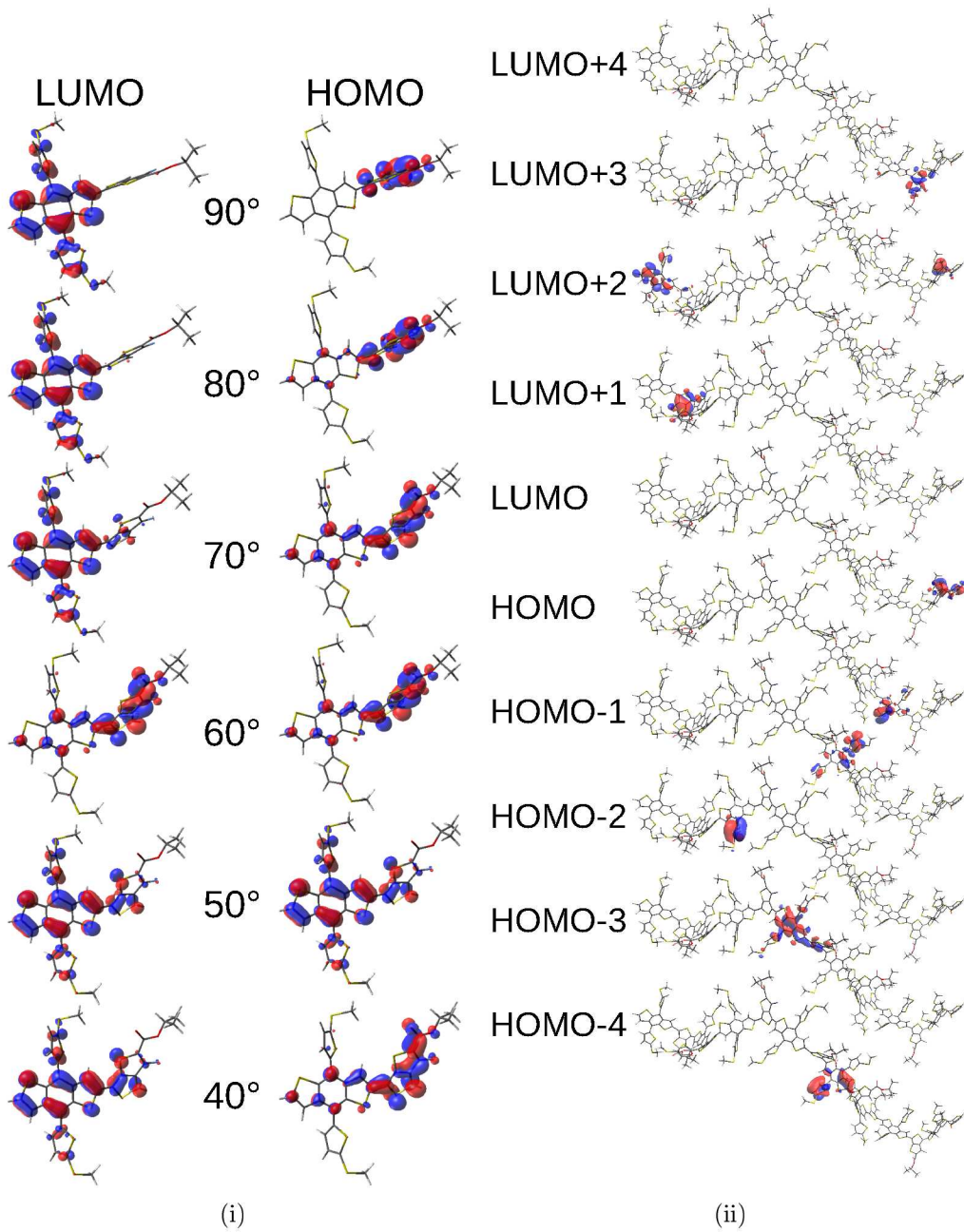


Figure A.27: (i) Frontier orbitals HOMO and LUMO on PBDT-TS1 monomer unit in an (AB)-linked structure. The structures are optimised in the electronic ground state on B3LYP/6-31G\* level of theory and the dihedral angle  $\theta(AB)$  is constrained ( $40^\circ, 50^\circ, 60^\circ, 70^\circ, 80^\circ$ ). The orbitals show that a cutoff dihedral angle  $\theta_{\text{cut}}(AB) \approx 60 - 70^\circ$  for the delocalised  $\pi$ -system results in a reasonable hopping site partitioning. (ii) Frontier orbitals HOMO-4 to LUMO+4 for PBDT-TS1 with chain length  $n = 8$  on PM3 level for an extracted from PBDT-TS1:PPDI blend.

### A.3.1 Internal Reorganization Energy

Table A.4: Internal reorganization energy  $\lambda_e^{\text{in}}$  and site-energy difference  $\Delta E_e^{\text{in}}$  for electron transport in PBDT-TS1 subunits the thienothiophene-based unit (**A**) and PBDT (**B**) for different functionals in eV.

functional/basis set	$\lambda_e^{\text{in}}(A \rightarrow B)$ [eV]	$\lambda_e^{\text{in}}(B \rightarrow A)$ [eV]	$\Delta E_e^{\text{in}}(A \rightarrow B)$ [eV]
BLYP / 6-311G**	0.516	0.464	0.401
B3LYP/6-31G*	0.581	0.539	0.317
B3LYP/6-311G**	0.644	0.569	0.271
CAM-B3LYP/6-311G**	0.779	0.704	0.129
PBE0/6-31G*	0.586	0.546	0.358

Table A.5: Internal reorganization energy  $\lambda_h^{\text{in}}$  and site-energy difference  $\Delta E_h^{\text{in}}$  for hole transport in PBDT-TS1 subunits the thienothiophene-based unit (**A**) and PBDT (**B**) for different functionals in eV.

functional/basis set	$\lambda_h^{\text{in}}(A \rightarrow B)$ [eV]	$\lambda_h^{\text{in}}(B \rightarrow A)$ [eV]	$\Delta E_h^{\text{in}}(A \rightarrow B)$ [eV]
BLYP/6-311G**	0.613	0.412	1.385
B3LYP/6-31G*	0.602	0.454	1.327
B3LYP/6-311G**	0.646	0.492	1.278
CAM-B3LYP/6-311G**	0.637	0.601	1.058
PBE0/6-31G*	0.618	0.442	1.311

Table A.6: Internal reorganization energy  $\lambda_h^{\text{in}}$  for hole transfer on PBE0/6-31G\* level in eV. The charge transfer occurs from molecule / hopping site A (line) to a target molecule / hopping site B (column).

The following numbers label the molecules 1) PPDI-H 2) PPDI-R including the side chains and PBDT-TS1 polymer units 3) thienothiophene-based unit (**A**) 4) PBDT (**B**) 5)  $A_1B_1$  6)  $A_2B_2$  7)  $A_3B_3$  8)  $A_4B_4$

$A \rightarrow B$	1	2	3	4	5	6	7	8
1	0.083	0.084	0.177	0.514	0.402	0.179	0.158	0.131
2	0.084	0.085	0.178	0.515	0.403	0.180	0.159	0.132
3	0.187	0.188	0.280	0.618	0.505	0.283	0.261	0.234
4	0.348	0.349	0.442	0.779	0.667	0.444	0.423	0.396
5	0.300	0.301	0.394	0.731	0.619	0.396	0.375	0.347
6	0.166	0.167	0.260	0.597	0.485	0.262	0.241	0.214
7	0.143	0.144	0.237	0.574	0.462	0.239	0.218	0.191
8	0.123	0.124	0.216	0.554	0.441	0.219	0.197	0.170

Table A.7: Internal reorganization energy  $\lambda_e^{\text{in}}$  for electron transfer on PBE0/6-31G\* level of theory in eV.

The charge transfer occurs from molecule / hopping site A (line) to a target molecule / hopping site B (column).

The following numbers label the molecules 1) PPDI-H 2) PPDI-R including the side chains and PBDT-TS1 polymer units 3) thienothiophene-based unit (**A**) 4) PBDT (**B**) 5) A<sub>1</sub>B<sub>1</sub> 6) A<sub>2</sub>B<sub>2</sub> 7) A<sub>3</sub>B<sub>3</sub> 8) A<sub>4</sub>B<sub>4</sub>

$A \rightarrow B$	1	2	3	4	5	6	7	8
1	0.136	0.138	0.360	0.362	0.242	0.216	0.194	0.170
2	0.138	0.140	0.363	0.365	0.245	0.218	0.197	0.172
3	0.360	0.362	0.584	0.586	0.466	0.440	0.418	0.394
4	0.321	0.323	0.546	0.548	0.428	0.401	0.380	0.355
5	0.229	0.231	0.454	0.456	0.336	0.309	0.288	0.263
6	0.194	0.196	0.419	0.421	0.301	0.274	0.253	0.228
7	0.174	0.176	0.399	0.401	0.281	0.254	0.233	0.208
8	0.157	0.159	0.382	0.384	0.264	0.237	0.216	0.192

Table A.8: Internal site-energy difference for hole transfer  $\Delta E_h^{\text{in}}$  and electron transfer  $\Delta E_e^{\text{in}}$  on PBE0/6-31G\* level of theory. The charge transfer occurs from molecule / hopping site A (line) to a target molecule / hopping site B (column).

The following numbers label the molecules 1) PPDI-H 2) PPDI-R including the side chains and PBDT-TS1 polymer units 3) thienothiophene-based unit (**A**) 4) PBDT (**B**) 5) A<sub>1</sub>B<sub>1</sub> 6) A<sub>2</sub>B<sub>2</sub> 7) A<sub>3</sub>B<sub>3</sub> 8) A<sub>4</sub>B<sub>4</sub>

$\Delta E_h^{\text{in}} / \text{eV}$								
$A \rightarrow B$	1	2	3	4	5	6	7	8
1	0.000	-0.032	0.595	-0.717	-0.897	-1.174	-1.357	-1.498
2	0.032	0.000	0.627	-0.684	-0.865	-1.142	-1.325	-1.466
3	-0.595	-0.627	0.000	-1.311	-1.492	-1.769	-1.952	-2.092
4	0.717	0.684	1.311	0.000	-0.180	-0.457	-0.641	-0.781
5	0.897	0.865	1.492	0.180	-0.000	-0.277	-0.460	-0.601
6	1.174	1.142	1.769	0.457	0.277	0.000	-0.184	-0.324
7	1.357	1.325	1.952	0.641	0.460	0.184	0.000	-0.140
8	1.498	1.466	2.092	0.781	0.601	0.324	0.140	0.000
$\Delta E_e^{\text{in}} / \text{eV}$								
$A \rightarrow B$	1	2	3	4	5	6	7	8
1	0.000	-0.000	2.300	1.942	1.503	0.728	0.456	0.350
2	-0.000	0.000	2.300	1.942	1.503	0.728	0.456	0.350
3	-2.300	-2.300	0.000	0.358	-0.797	-1.573	-1.845	-1.951
4	-1.942	-1.942	0.358	0.000	-0.439	-1.214	-1.487	-1.593
5	-1.503	-1.503	0.797	0.439	0.000	-0.775	-1.048	-1.154
6	-0.728	-0.728	1.573	1.214	0.775	0.000	-0.272	-0.378
7	-0.456	-0.456	1.845	1.487	1.048	0.272	0.000	-0.106
8	-0.350	-0.350	1.951	1.593	1.154	0.378	0.106	0.000

## A.4 PDTI

Table A.9: Characteristic structure parameters for the optimised ground state  $S_0$  geometries for the enantiomers cis-PDTI-A and cis-PDTI-B on PBE0-D3(BJ)/6-31G\* level in  $\text{CHCl}_3$  solution. The dihedral angle  $\theta_1(\text{C}^{43}-\text{C}^{15}-\text{C}^{52}-\text{C}^{19})$  takes the relative orientation of both PDI units into account (see Fig. 5.15). The distance between the adjacent nitrogen atoms on two PDI subunits is  $d_2(\text{N}^{36}-\text{N}^{54})$ . The intramolecular distance for the PDI stacks is characterised by the distance  $d_1(\text{C}^{15}-\text{C}^{52})$ .  $d_3(\text{O}^{59}-\text{O}^{65})$  is the distance between the outer oxygen atoms on the PDI units. The superscript number refers to the atomic index.

	cis-PDTI-A	cis-PDTI-B
$\theta_1(\text{C}^{43}-\text{C}^{15}-\text{C}^{52}-\text{C}^{19})$	$130.9^\circ$	$-135.7^\circ$
$d_1(\text{C}^{15}-\text{C}^{52})$	2.81 Å	2.83 Å
$d_2(\text{N}^{36}-\text{N}^{54})$	4.62 Å	4.92 Å
$d_3(\text{O}^{59}-\text{O}^{65})$	4.03 Å	4.08 Å

## A.5 PHHP-AS

Table A.10: Characteristic structure parameters for the optimised ground state  $S_0$  geometries for the enantiomers PHHP-*P* and PHHP-*M* on PBE0-D3(BJ)/6-31G\* level in  $\text{CHCl}_3$  solution. The dihedral angles  $\theta_1$  and  $\theta_2$  take the relative orientation of the PDI units into account. The intramolecular distance for the PDI stacks is characterised with the distances  $d_1$  and  $d_2$ .  $d_3$  is the distance between the inner oxygen atoms on the PDI units.

	PHHP- <i>P</i>	PHHP- <i>M</i>
$\theta_1$	$20.57^\circ$	$-20.57^\circ$
$\theta_2$	$14.66^\circ$	$-14.66^\circ$
$d_1$	3.39 Å	3.39 Å
$d_2$	3.21 Å	3.21 Å
$d_3$	4.20 Å	4.20 Å

Table A.11: Reorganization energy for hole transfer  $\lambda_h^{\text{in}}$  and for electron transfer  $\lambda_e^{\text{in}}$  for PHHP-*P* and PHHP-*M* on PBE0-D3(BJ)/6-31G\* level of theory. The reorganization energies for hole transport are slightly higher than those for electron transport.

	$\lambda_h^{\text{in}} / \text{eV}$	$\lambda_e^{\text{in}} / \text{eV}$
PHHP- <i>P</i> → PHHP- <i>P</i>	0.159	0.146
PHHP- <i>M</i> → PHHP- <i>M</i>	0.150	0.146
PHHP- <i>P</i> → PHHP- <i>M</i>	0.155	0.146
PHHP- <i>M</i> → PHHP- <i>P</i>	0.154	0.146

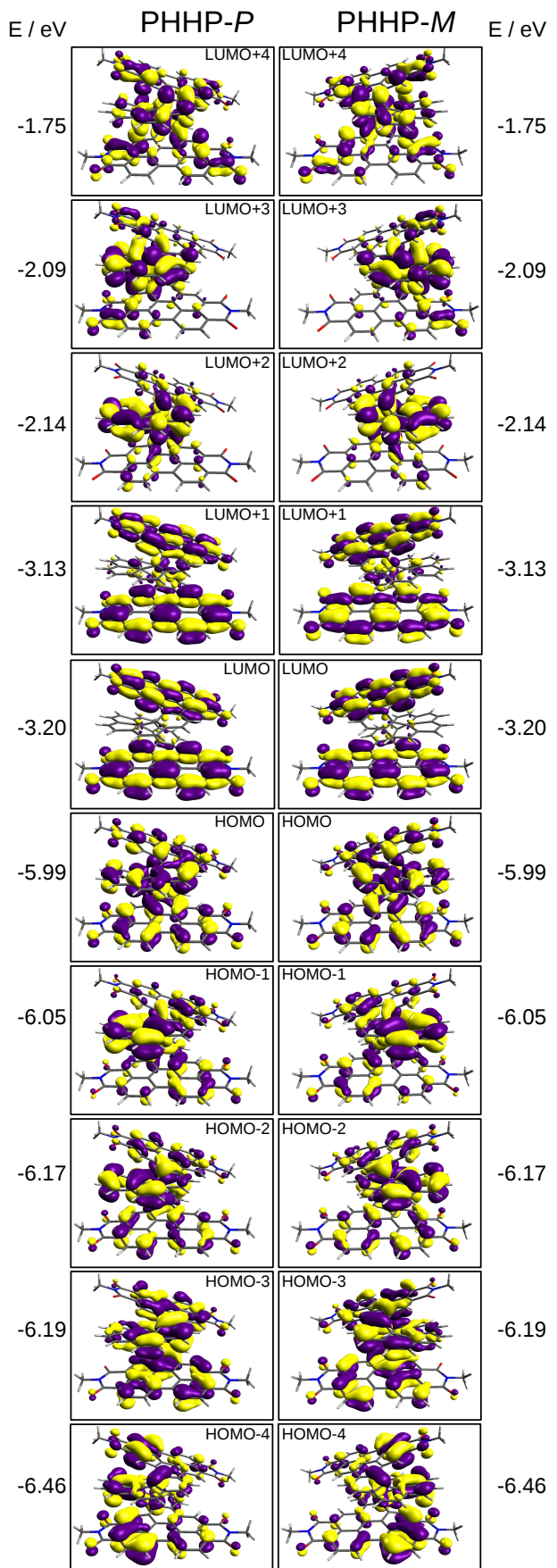


Figure A.28: Frontier orbitals and Kohn-Sham orbital energies for the enantiomers PHHP-*P* and PHHP-*M* on PBE0-D3(BJ)/6-31G\* level in CHCl<sub>3</sub> solution.

## A.6 PDI-Pyr

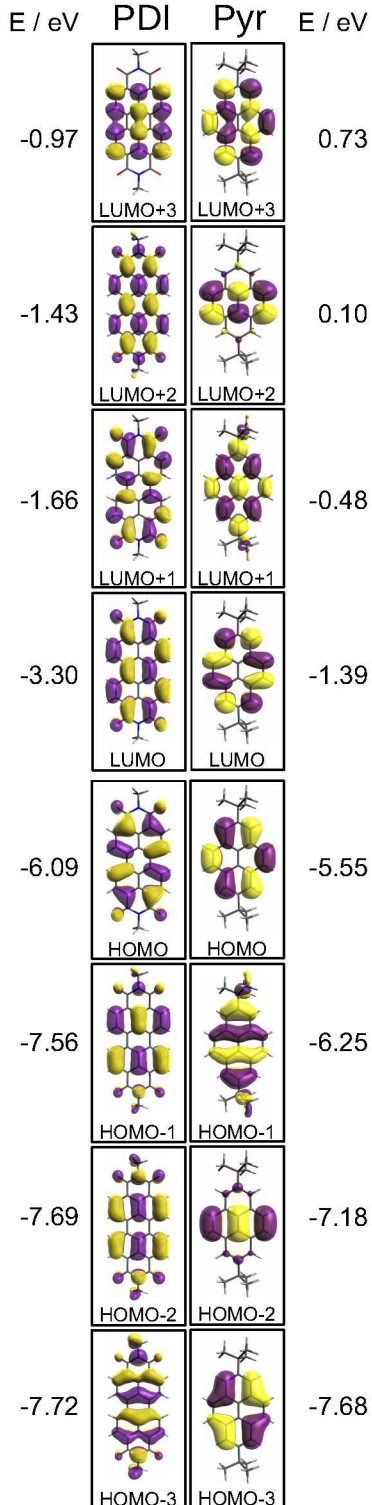


Figure A.29: Frontier orbitals and Kohn-Sham energies of the building blocks PDI and Pyrene (Pyr) in  $\text{CHCl}_3$  on PBE0-D3(BJ)/6-31G\* level with PCM and Bondi radii.

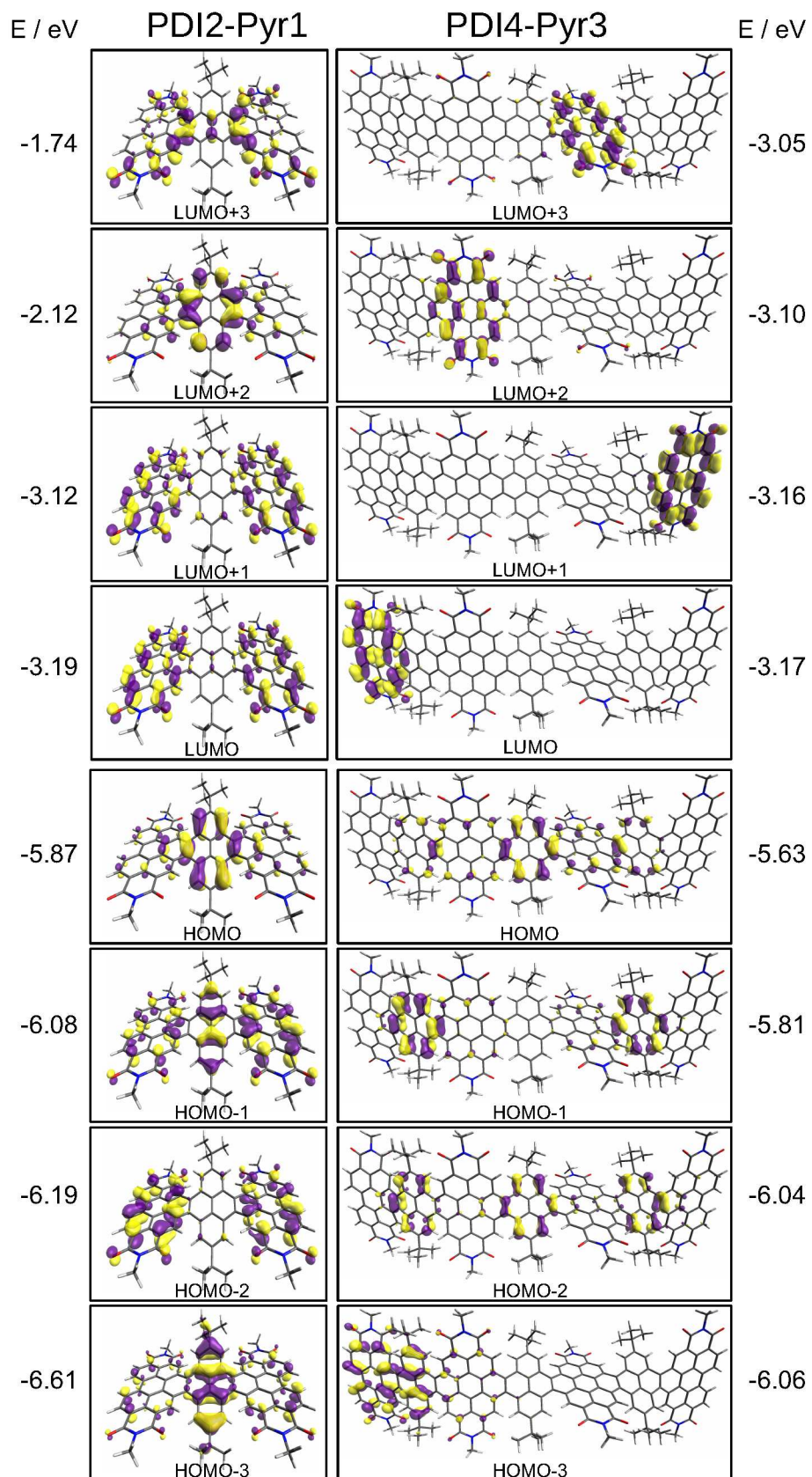


Figure A.30: Frontier orbitals and Kohn-Sham energies of PDI2-Pyr1 and PDI4-Pyr3 in CHCl<sub>3</sub> on PBE0-D3(BJ)/6-31G\* level with PCM and Bondi radii.

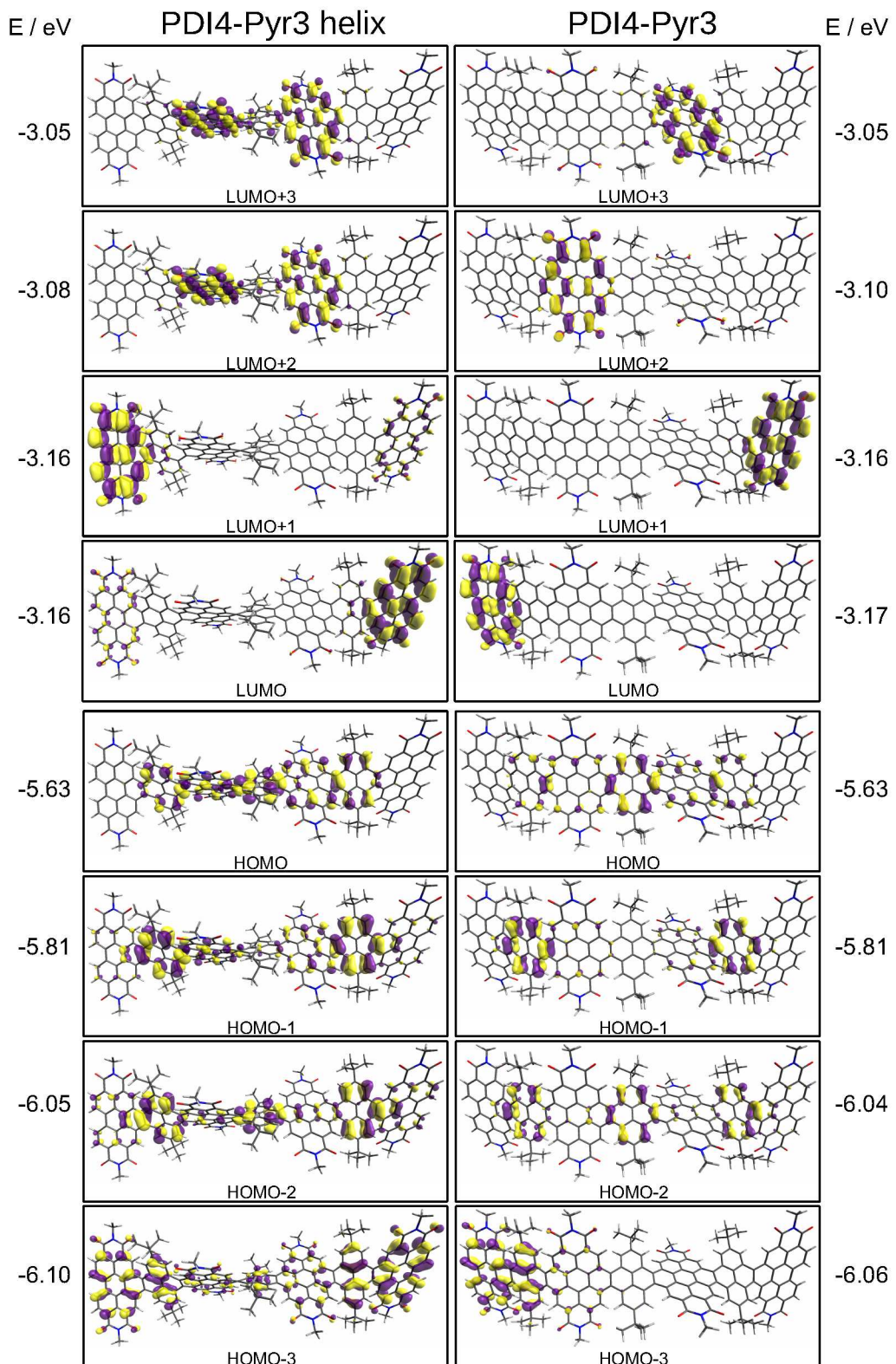


Figure A.31: Frontier orbitals and Kohn-Sham energies of helical *P*-PDI4-Pyr3 and PDI4-Pyr3 in CHCl<sub>3</sub> on PBE0-D3(BJ)/6-31G\* level with PCM and Bondi radii.

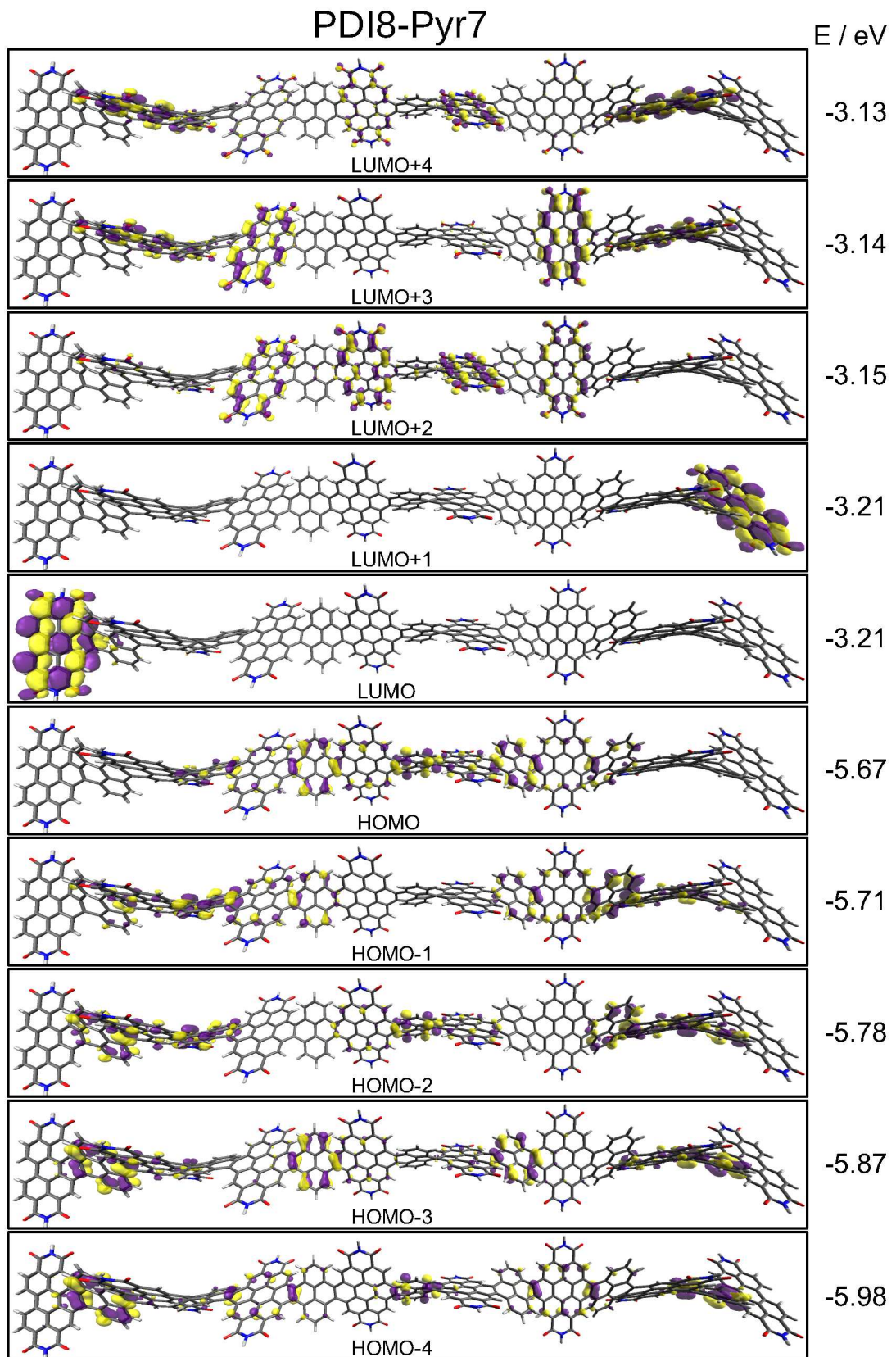


Figure A.32: Frontier orbitals and Kohn-Sham energies of helical *P*-PDI8-Pyr7 in CHCl<sub>3</sub> on PBE0-D3(BJ)/6-31G\* level with PCM and Bondi radii.

## A.7 Pt Complexes

Table A.12: Bond angles  $\phi_1(\text{N8-Pt1-N15})$ ,  $\phi_2(\text{C1-Pt1-C21})$  and dihedral angles  $\theta_1(\text{C12-N13-C31-C32})$  of monomers **C1** to **C6** in the crystal and at the optimised  $S_0$  and  $T_1$  geometries in THF matrix.

		Crystal	$S_0$	$T_1$
<b>C1</b>	$\phi_1$	92.3	93.0	92.5
	$\phi_2$	103.9	103.5	102.5
	$\theta_1$	-91.4	-84.4	-86.3
<b>C2</b>	$\phi_1$		93.2	92.7
	$\phi_2$		103.3	102.5
	$\theta_1$		-84.9	-86.0
<b>C3</b>	$\phi_1$	93.9	94.1	93.7
	$\phi_2$	102.9	102.8	102.2
	$\theta_1$	-87.5	-83.5	-85.2
<b>C4</b>	$\phi_1$		94.0	93.5
	$\phi_2$		103.0	102.2
	$\theta_1$		-83.5	-85.2
<b>C5</b>	$\phi_1$	93.0	93.9	93.3
	$\phi_2$	103.4	102.5	102.4
	$\theta_1$	91.1	95.4	94.8
<b>C6</b>	$\phi_1$	91.5	92.5	92.5
	$\phi_2$	102.9	102.6	100.9
	$\theta_1$	-85.6	-89.9	-90.0

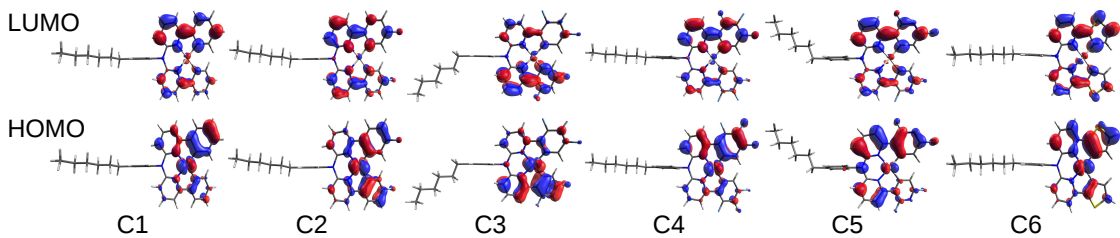


Figure A.33: Frontier orbitals HOMO and LUMO of the isolated monomers of complexes **C1** to **C6** at the optimised  $T_1$  geometry and with highest contributions to the  $T_1 \rightarrow S_0$  transition as obtained by means of (TD)DFT.

The internal energy difference for charge transfer based on CDFT calculations is depicted in (Fig. A.34).

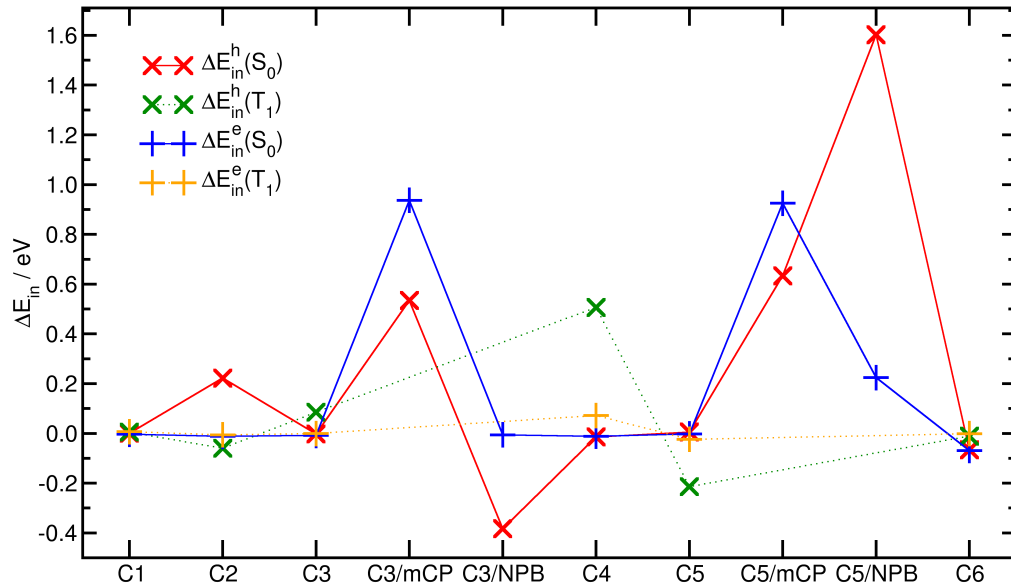


Figure A.34: CDFT-based vertical energy gap  $\Delta E_{in}$  for dimer structures of Pt complexes **C1**, **C2**, **C3**, **C4**, **C5**, **C6** and hetero-molecular charge-transfer pairs **C3/mCP**, **C3/NPB**, **C5/mCP**, **C5/NPB**. Comparison of geometries in the ground state  $S_0$  and excited triplet state  $T_1$  geometries for hole transfer (red, green) and electron transfer (blue, orange). For homo-molecular dimers the energy difference  $\Delta E_{in}$  is close to zero, whereas they may differ for hetero-molecular dimer conformations.





## A.8 Abbreviations

3OB-3-1	third-order parametrisation for organic and biological systems
6-31G*	Pople basis set
AM1	Austin model 1
B3LYP	hybrid functional by Becke, Lee, Yang and Parr
BDT	benzo[1,2-b:4,5-b']dithiophene
BHJ-OSC	Bulk heterojunction organic solar cell
BJ	Becke-Johnson damping
BLYP	functional by Becke, Lee, Yang and Parr
CAM-B3LYP	functional B3LYP with a Coulomb-attenuating method
CDFT	constrained density functional theory
CG	coarse-grained
CI	configuration interaction
CNDO	complete neglect of differential overlap
COM	centre of mass
CV	cyclic voltammetry
CX	platinum complex number X (Fig. 6.1)
D2, D3, D4	Grimme's dispersion correction
D3(BJ)	Grimme's dispersion correction with Becke-Johnson damping
DFT	density functional theory
DFTB	density functional tight binding
DFTB3	third order density functional tight binding
DIPBI	tetrachlorinated diperylene bisimide
DIPRO	dimer projection method
DONOR:ACCEPTOR	blend morphology with donor and acceptor materials
DONOR/ACCEPTOR	charge transfer pair with donor and acceptor site
DONOR→ACCEPTOR	charge transfer direction of a single transition
EA	electron affinity
ECD	electronic circular dichroism
EIL	electron injection layer
EML	emission layer
ESP	electrostatic potential
ETL	electron transport layer
FEM	field-effect mobility
FF	force field
GDOS	gaussian density of states
GIAO	gauge-independent atomic orbital
HDI	hexacene diimide
HF	Hartree-Fock
HH	hexapole helicene
HIL	hole injection layers
HOMO	highest occupied molecular orbital
HTL	hole transport layer
INDO	intermediate neglect of differential overlap
IP	ionisation potential
ISC	intersystem crossing
ITO	indium tin oxide
kMC	kinetic Monte Carlo
KS	Kohn-Sham
LC	long-range correction
LED	liquid crystal display

LUMO	lowest unoccupied molecular orbital
MA	minimal appearing distance
mCP	1,3-bis(carbazol-9-yl)benzene
MD	molecular dynamics
MM	molecular mechanics
MMA	mean minimal appearing distance
MNDO	modified neglect of diatomic overlap
MIO-1-1	DFTB parameter set
MO	molecular orbital
MOO	molecular orbital overlap
NPB	N,N'-bis(naphthalen-1-yl)-N,N'-bis(phenyl)benzidine
NDI	naphthalene diimide
OFET	organic field-effect transistor
OSC	organic solar cell
OLED	organic light emitting diode
P3HT	poly(3-hexyl-thiophene)
P3MT	poly(3-methyl-thiophene)
PBE	functional by Perdew, Burke and Ernzerhof
PBE0	Hybrid functional by Perdew, Burke and Ernzerhof
PBI	perylene bisimide
PCE	power conversion efficiency
PCM	polarisable continuum model
PDI	perylene diimide
PPDI	nonplanar dimeric PBI derivative (Fig. 5.1,3)
PPD	pentaperylene decaimides
PPD-Se	selenium-annulated pentaperylene decaimides
PDI-Pyr	laddered graphene nanoribbons consisting of perylene diimide and pyrene units
PDTTI	acceptor molecule (Fig. 5.1,9)
PHHP-AS	acceptor molecule (Fig. 5.1,10)
PM3	parametric method number 3
PW	plane wave
Pyr	pyrene
QM	quantum mechanics
RCOM	aromatic ring-based centre of mass
SCF	self-consistent field
SI	supporting information
SOC	spin-orbit coupling
STO	Slater-type orbital
STO- <i>n</i> G	minimal basis sets, <i>n</i> primitive gaussian orbitals are fitted to a single STO.
TDDFT	time-dependent density functional theory
TDI	tetracene diimide
THF	tetrahydrofuran
TPBI	1,3,5-tris(1-phenyl-1H-benzo[d]imidazole-2-yl)benzene
TPH	triperylene hexaimides
TPH-Se	selenium-annulated triperylene hexaimides
UV-Vis	ultraviolet-visible
UV-Vis-NIR	ultraviolet-visible near-infrared
UFF	universal force field
ZFS	zero-field splitting
ZDO	zero differential overlap approximation
ZINDO	Zerner's intermediate neglect of differential overlap

## Acknowledgements

Fortunately, I received tremendous support for this thesis from many people, without whom it would not have been possible. First of all, I want to thank my supervisor Prof. Dr. Nikos Doltsinis, who made this thesis possible in the first place and for his continuous support and guidance throughout the last years in research. Furthermore, I would like to express my sincere thanks to Prof. Dr. Andreas Heuer for taking on the role of second reviewer and to Prof. Dr. Cornelia Denz for taking on the role of third reviewer.

I am indebted to Jim Bachmann for his enormous efforts on the multiscale and kinetic Monte Carlo approach and fruitful scientific discussions. Moreover, I express my gratitude to Dr. Christian Schwermann and Thorsten Winands for scientific and IT support on versatile programming issues. Besides, I appreciate the time and consideration from Dr. Marcus Böckmann for providing valuable help on electronic structure theory and molecular mechanics simulations. Furthermore, I want to thank Tobias Lettmann for his assistance, especially the introduction to CDFT and Frank Lengers, to contribute to the DIPRO module. I am also thankful to Dana Brünink, Marvin Nyenhuis, Helena Osthues, Timmy Ly, Dr. Huu-Chuong Nguyen, Christopher Hodde and all the present and former members of the group for creating an outstanding and harmonic working atmosphere.

Huge parts of this thesis would not have been possible without collaborations. Especially, I want to thank Prof. Dr. Cristian Strassert and his group for cooperations on OLED materials, fruitful discussions and valuable experimental insights. I extend particular thanks to Prof. Dr. Yan Li, Guogang Liu and Xiaoping Cui for collaboration on projects concerning organic solar cells and organic field-effect transistors. I want to take this opportunity to thank Dr. Cristiane Höppener and Paul Popp for their collaboration on a project concerning photoluminescent metal-organic complexes containing ruthenium centres. Particularly, I thank Franco Bonafé for assistance concerning DFTB+. I am grateful for the enormous support from Stephan Majert and Matthias Kemper.

This project was partially funded by NSFC-DFG joint project PAK943-TRR61 (21661132006). I am thankful for technical support and simulation time at the high-performance computing facilities (PALMA) at WWU Münster. Finally, I want to thank my family and friends for their unconditional love and support during every year of my life.